AGU PUBLICATIONS

JGR

Journal of Geophysical Research: Solid Earth

RESEARCH ARTICLE
10.1002/2015JB012200

Key Points:
- Thermal decomposition can contribute substantial dynamic weakening
- Thermal decomposition leads to longer rupture durations and larger slips
- Thermal pressurization and decomposition can combine in multiple ways to propagate a slip pulse

Correspondence to:
J. D. Platt,
jplatt@seas.harvard.edu

Citation:
Platt, J. D., R. C. Viesca, and D. I. Garagash (2015), Steadily propagating slip pulses driven by thermal decomposition, *J. Geophys. Res. Solid Earth*, *120*, doi:10.1002/2015JB012200.

Received 13 MAY 2015
Accepted 12 AUG 2015
Accepted article online 17 AUG 2015

Steadily propagating slip pulses driven by thermal decomposition

John D. Platt[1,2], Robert C. Viesca[3,4], and Dmitry I. Garagash[3]

[1]School of Engineering and Applied Sciences, Harvard University, Cambridge, Massachusetts, USA, [2]Now at Department of Terrestrial Magnetism, Carnegie Institution for Science, Washington, District of Columbia, USA, [3]Department of Civil and Resource Engineering, Dalhousie University, Halifax, Nova Scotia, Canada, [4]Now at Department of Civil and Environmental Engineering, Tufts University, Medford, Massachusetts, USA

Abstract Geophysical observations suggest that mature faults weaken significantly at seismic slip rates. Thermal pressurization and thermal decomposition are two mechanisms commonly used to explain this dynamic weakening. Both rely on pore fluid pressurization with thermal pressurization achieving this through thermal expansion of native solids and pore fluid and thermal decomposition by releasing additional pore fluid during a reaction. Several recent papers have looked at the role thermal pressurization plays during a dynamically propagating earthquake, but no previous models have studied the role of thermal decomposition. In this paper we present the first solutions accounting for thermal decomposition during dynamic rupture, solving for steady state self-healing slip pulses propagating at a constant rupture velocity. First, we show that thermal decomposition leads to longer slip durations, larger total slips, and a distinctive along–fault slip rate profile. Next, we show that accounting for more than one weakening mechanism allows multiple steady slip pulses to exist at a given background stress, with some solutions corresponding to different balances between thermal pressurization and thermal decomposition, and others corresponding to activating a single reaction multiple times. Finally, we study how the rupture properties depend on the fault properties and show that the impact of thermal decomposition is largely controlled by the ratio of the hydraulic and thermal diffusivities $\chi = \alpha_{hy}/\alpha_{th}$ and the ratio of pore pressure generated to temperature rise buffered by the reaction P_r/E_r.

1. Introduction

Several lines of evidence suggest that mature faults weaken significantly at seismic slip rates. First, the background stress resolved on mature faults is often low [*Townend and Zoback*, 2004], suggesting that for an earthquake to propagate the fault must experience a significant coseismic strength drop from a peak strength consistent with Byerlee's law [*Byerlee*, 1978]. Second, the lack of an observable heat anomaly on major faults [*Lachenbruch and Sass*, 1980; *Fulton et al.*, 2013]—and the scarcity of frictional melt products—suggests that the fault strength during seismic slip is much less than the strength predicted by Byerlee's law. Finally, high-velocity friction experiments performed on natural samples show a sharp drop in friction coefficient for slip rates above ~0.1 m/s [*Di Toro et al.*, 2011], which is an order of magnitude lower than typical seismic slip rates of ~1 m/s.

Several mechanisms have been proposed to explain this dynamic weakening. In this paper we will focus on just two of these mechanisms, thermal pressurization and thermal decomposition. Both mechanisms rely on elevated pore fluid pressures in a fluid-saturated gouge layer, with thermal pressurization achieving this through thermal expansion of native pore fluid and thermal decomposition by releasing additional pore fluid—for example, H_2O or CO_2—during a devolatilization reaction. For typical conditions within the seismogenic zone these reactions are endothermic, and at a fixed pressure the reaction products occupy a larger volume than the reactants, leading to pore pressure increases and thus weakening as the reaction progresses. Thermal decomposition reactions are ubiquitous among common fault materials with experimental evidence for decomposition of calcite [*Han et al.*, 2007a; *Smith et al.*, 2013], siderite [*Han et al.*, 2007b], dolomite [*De Paola et al.*, 2011], serpentinites [*Hirose and Bystricky*, 2007; *Proctor et al.*, 2014], kaolinite [*Brantut et al.*, 2008], and gypsum [*Brantut et al.*, 2011]. The activation of thermal decomposition has also been inferred in field observations of natural carbonate faults [*Collettini et al.*, 2013; *Bullock et al.*, 2014]. Other proposed

weakening mechanisms exist, such as flash heating [e.g., *Rice*, 1999, 2006; *Goldsby and Tullis*, 2011] or the as yet poorly understood weakening associated with nanometer-sized gouge particles, but we neglect these mechanisms in this paper, allowing us to study the balance between thermal pressurization and thermal decomposition in isolation.

Many theoretical studies have looked at the role of thermal pressurization during seismic slip. *Lachenbruch* [1980] solved for the slip-weakening distance and maximum temperature rise for a finite thickness gouge layer deforming under undrained and adiabatic conditions, showing that thermal pressurization leads to total coseismic weakening and a finite temperature rise. *Mase and Smith* [1985, 1987] and *Rice* [2006] extended the analysis in *Lachenbruch* [1980] to account for hydraulic and thermal diffusion into the adjacent material, solving for the shear strength and temperature evolution for slip on a mathematical plane. Finally, *Rempel and Rice* [2006] combined the two approaches, solving for a finite thickness shear zone during kinematically imposed slip while accounting for hydrothermal diffusion.

Recent work has gone beyond the kinematically imposed slip rates used in the previous references. *Garagash and Rudnicki* [2003] coupled a gouge layer undergoing thermal pressurization to a spring-slider model and *Andrews* [2002] presented the first model to couple thermal pressurization to an elastodynamic model for a propagating rupture, showing that thermal pressurization may lead to an almost total coseismic strength drop during large earthquakes. This was extended to account for additional frictional effects [*Bizzarri and Cocco*, 2006; *Noda et al.*, 2009] and incorporated into earthquake cycle simulations [*Noda and Lapusta*, 2010]. *Garagash* [2012] showed that thermal pressurization and the associated hydrothermal diffusion in the gouge and surrounding rock support self-healing pulse-like ruptures. Thermal pressurization is important when determining how a rupture evolves in a heterogeneous fault system. *Urata et al.* [2012] showed that accounting for thermal pressurization allows a rupture to jump a wider step over; *Noda and Lapusta* [2013] showed that thermal pressurization can weaken rate-strengthening sections of faults that would not normally slip seismically; *Urata et al.* [2014] showed that the efficiency of thermal pressurization is an important consideration when determining if a rupture can branch.

Theoretical studies of thermal decomposition have been far fewer than theoretical studies of thermal pressurization. *Sulem and Famin* [2009] and *Sulem et al.* [2009] (hereafter cited together as *Sulem et al.* [2009]), and *Brantut et al.* [2010] studied thermal decomposition in a gouge layer deforming in response to a kinematically imposed slip rate. They showed that the endothermic reaction limits the maximum temperature rise below a typical melting temperature, and the onset of the reaction accelerates dynamic weakening. *Brantut and Sulem* [2012] relaxed the constant slip rate constraint by coupling the gouge layer to a spring-slider model, and *Platt et al.* [2015] studied how thermal decomposition could drive coseismic strain localization. Finally, *Poulet et al.* [2014] studied how the thermal decomposition of serpentinite could lead to episodic tremor and slow slip.

In this paper we present the first dynamic rupture solutions to account for thermal decomposition. Building on the solutions for thermal pressurization alone from *Garagash* [2012], we solve for a steady state self-healing slip pulse propagating at a constant rupture velocity. We investigate the interplay between thermal pressurization and thermal decomposition and look for a distinctive signature of thermal decomposition that might be observable in seismic data. In addition, we determine the important fault properties that control the total weakening contributed by thermal decomposition. It is unlikely that ruptures often propagate as a steady slip pulse. However, steady slip pulses often mark the boundary between growing and decaying slip pulses [*Gabriel et al.*, 2012], a critical state that may select the conditions in which critically stressed faults operate. Steady pulses also provide a simple idealized case that allows the underlying physics to be probed in more detail than is typical for larger nonsteady rupture simulations.

Our decision to look for self-healing slip pulses is based on the seismological observations from *Heaton* [1990], which showed that in large earthquakes the slip duration at a point on a fault can be much shorter than the event duration. Furthermore, theoretical work has shown that slip pulse propagation is favored over expanding crack-like ruptures at the low background stresses thought to be resolved on mature faults [*Zheng and Rice*, 1998; *Noda et al.*, 2009]. Many previous studies have solved for steady slip pulses using a range of models for fault strength. These include *Yoffe* [1951], *Broberg* [1978], *Freund* [1979], *Perrin et al.* [1995], *Rice et al.* [2005], and *Garagash* [2012]. However, only a subset of these [*Perrin et al.*, 1995; *Garagash*, 2012] address the self-healing nature of a slip pulse, where the stress on the fault is required to be below the strength whenever the fault is not slipping.

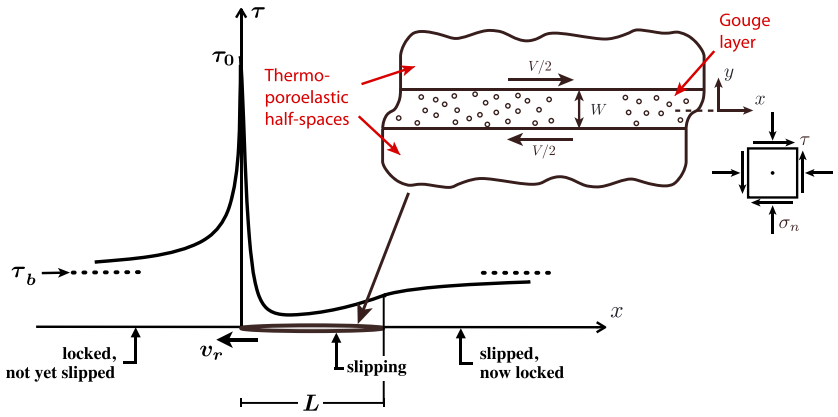

Figure 1. Plot showing the geometry used to solve for a slip pulse of length L propagating at a constant rupture velocity of v_r. The coordinate x is oriented parallel to the fault and is zero at the rupture tip; the coordinate y is oriented perpendicular to the fault and is zero at the center of the gouge layer where strain rates are highest. The stress rises from the background stress τ_b far ahead of the pulse to the initial strength τ_0 at the rupture tip, is equal to the shear strength of the gouge layer within the slipping portion of the fault, and then rebounds back to the background stress far behind the slip pulse. The shear strength at each point on the fault is calculated using a model for the deformation of a fluid-saturated gouge layer sheared between two undeforming thermoporoelastic half-spaces accounting for thermal pressurization and thermal decomposition. This figure is based upon Figure 1 from *Garagash* [2012] and Figure 1 from *Platt et al.* [2014].

2. Model for Steadily Propagating Slip Pulses

In this section we develop our model for a self-healing slip pulse traveling from right to left at a constant rupture velocity v_r with dynamic weakening driven by a combination of thermal pressurization and thermal decomposition. We consider a one-dimensional fault embedded in a two-dimensional elastic medium with the x coordinate running parallel to the fault and the y coordinate running perpendicular to the fault, as shown in Figure 1. Note that our solution for a steady state slip pulse implicitly assumes homogeneous fault properties. The elastodynamic portion of our model is based on *Weertman* [1980] and *Garagash* [2012]. Our model for thermal pressurization and thermal decomposition is based heavily on the models derived in *Sulem et al.* [2009] and *Brantut et al.* [2010] but uses the notation from *Platt et al.* [2015] to quantify the temperature rise buffered and pore pressure generated by thermal decomposition.

2.1. Conservation of Energy

Using the notation from *Platt et al.* [2015] we can write the conservation of energy at any point on the fault as

$$\frac{\partial \theta}{\partial t} = \frac{\tau_f \dot{\gamma}}{\rho c} + \alpha_{\text{th}} \frac{\partial^2 \theta}{\partial y^2} - \bar{m} E_r \frac{\partial \xi}{\partial t}, \tag{1}$$

where θ is fault temperature, ρc is the effective heat capacity per unit reference volume, α_{th} is the thermal diffusivity, τ_f is the shear strength of the gouge layer, $\dot{\gamma}$ is the strain rate within the gouge layer, ξ is the reaction extent, $\bar{m}$ is the initial reactant mass fraction within the gouge layer, and E_r is the total temperature rise buffered by a completed reaction in a pure material. The definition of E_r can be found in *Platt et al.* [2015].

Each term in equation (1) has a clear physical meaning. The first term on the right-hand side models frictional heating in the gouge layer, the second term models thermal diffusion, and the final term models the latent heat associated with the endothermic reaction. Here we have neglected the work done by the normal stresses and the small heat flux associated with pore fluid flow, a common assumption that is justified for typical fault gouge permeabilities [*Mase and Smith*, 1985, 1987]. We have also assumed that ρc, α_{th} and E_r do not change with temperature and pore pressure.

The importance of thermal decomposition at a given location within the slip pulse is determined by the reaction kinetic, which controls how fast the reaction progresses. We model the reaction rate using a first-order reaction kinetic with an Arrhenius temperature dependence,

$$\frac{\partial \xi}{\partial t} = A(1-\xi)\exp\left(-\frac{Q}{R\theta}\right). \tag{2}$$

For simplicity we neglect reactant depletion—a good assumption for high initial reactant mass fractions or reactions with a large value of E_r—which is equivalent to setting $\xi \ll 1$ in equation (2). Next we assume that the reaction kinetic can be approximated as the product of the reaction rate in the middle of the gouge layer and a Gaussian function in y,

$$\frac{\partial \xi}{\partial t} = A \exp\left(-\frac{Q}{R\theta_{\mathrm{mp}}}\right) \exp\left(-\frac{\pi \beta^2 y^2}{W^2}\right), \tag{3}$$

where $\theta_{\mathrm{mp}}(t) = \theta|_{y=0}$ is the temperature at the midplane of the deforming zone. This assumption about the shape of the reacting zone is motivated by the common approximation used to model frictional heating within the gouge layer, where the shear strength of the gouge layer is evaluated using the pore pressure at the center of the deforming zone and the strain rate is assumed to have a fixed shape. Without this assumption it would be impossible to leverage the Green's function approach used in *Garagash* [2012]. The additional factor β is included in equation (3) to allow the reacting zone to have a different thickness than the deforming zone, and β is equal to the ratio between the deforming zone thickness W and the reacting zone thickness. As shown in Appendix C, we validate the approximations made in equation (3) using a numerical method that makes no assumptions about the reacting zone shape and use these tests to select an optimal value of β.

Equation (1) is converted to a frame moving with the slip pulse, which propagates from right to left with the rupture tip at $x = 0$, using the transformation

$$\frac{\partial}{\partial t} \rightarrow v_r \frac{\partial}{\partial x}. \tag{4}$$

Combining this transformation with the simplified reaction kinetic from equation (3), we arrive at the final equation modeling the conservation of energy,

$$v_r \frac{\partial \theta}{\partial x} = \frac{\tau_f \dot{\gamma}}{\rho c} + \alpha_{\mathrm{th}} \frac{\partial^2 \theta}{\partial y^2} - \bar{m} E_r A \exp\left(-\frac{Q}{R\theta_{\mathrm{mp}}}\right) \exp\left(-\frac{\pi \beta^2 y^2}{W^2}\right). \tag{5}$$

2.2. Conservation of Pore Fluid Mass

Using the notation from *Platt et al.* [2015], we can write the conservation of pore fluid mass at any point on the fault as

$$\frac{\partial p}{\partial t} = \Lambda \frac{\partial \theta}{\partial t} + \alpha_{\mathrm{hy}} \frac{\partial^2 p}{\partial y^2} + \bar{m} P_r \frac{\partial \xi}{\partial t}, \tag{6}$$

where p is the pore pressure, Λ is the thermal pressurization coefficient, α_{hy} is the hydraulic diffusivity, and P_r is the total pore pressure rise generated by a completed reaction in a pure material at constant temperature and undrained conditions. The first term on the right-hand side models thermal pressurization, the second term models hydraulic diffusion, and the final term models the pore pressure generated by thermal decomposition. We have assumed that the hydraulic properties are constant and thus do not change with temperature, pore pressure, or reaction extent. As before, we transform equation (6) to a frame moving with the slip pulse and approximate the reaction kinetic as the product of the reaction kinetic evaluated using the temperature at the center of the deforming zone and a Gaussian function in y. This leads to the final equation for the conservation of pore fluid mass

$$v_r \frac{\partial p}{\partial x} = v_r \Lambda \frac{\partial \theta}{\partial x} + \alpha_{\mathrm{hy}} \frac{\partial^2 p}{\partial y^2} + \bar{m} P_r A \exp\left(-\frac{Q}{R\theta_{\mathrm{mp}}}\right) \exp\left(-\frac{\pi \beta^2 y^2}{W^2}\right). \tag{7}$$

Different terms in equation (7) will be important at different locations within the slip pulse. Initially, thermal decomposition can be neglected and all weakening comes from thermal pressurization. If the reaction is triggered the results in *Sulem et al.* [2009] and *Brantut et al.* [2010] suggest that the onset of thermal decomposition will lead to an acceleration in dynamic weakening. Near the trailing edge of the slip pulse hydrothermal diffusion will lower the pore pressure, providing the restrengthening mechanism that allows self-healing slip pulses to occur.

2.3. Deformation Within the Gouge Layer

Rice [2006] suggested that inertial effects within the gouge layer will be negligible during seismic shear due to the small distances over which hydraulic and thermal diffusion act. This hypothesis was tested in *Platt et al.* [2014] and found to be true for typical seismogenic conditions, with the possible exception of the rupture tip

where slip rates can be large. Neglecting inertia within the gouge layer allows us to write the conservation of momentum using the conditions for mechanical equilibrium,

$$\frac{\partial \tau}{\partial y} = 0 \quad , \quad \frac{\partial \sigma_n}{\partial y} = 0, \tag{8}$$

where τ is the shear stress on the fault and σ_n is the normal stress on the fault, which is assumed to be constant.

The shear strength within the gouge layer is controlled by a friction coefficient f and the Terzaghi effective stress,

$$\tau_f = f(\sigma_n - p). \tag{9}$$

It is important to note that when the gouge is deforming, and thus the stress on the fault is equal to the gouge layer strength, equation (9) is incompatible with equation (8) if the friction coefficient is assumed to be constant. Only two forms of deformation are possible, uniform shear of the gouge under undrained and adiabatic conditions or slip on the plane of maximum pore pressure [*Rice*, 2006]. If the friction coefficient varies across the gouge layer, then a localized zone with a finite thickness can develop, but this thickness may vary dramatically during seismic slip [*Rice et al.*, 2014; *Platt et al.*, 2014, 2015] and should be determined as part of the solution. However, such a calculation is far beyond the scope of this paper, and we ignore the complications associated with strain rate localization by assuming that the deforming zone has a Gaussian shape with constant width W,

$$\dot{\gamma} = \frac{V(x)}{W} \exp\left(-\frac{\pi y^2}{W^2}\right), \tag{10}$$

where V is the slip rate accommodated across the gouge layer. Fixing the deforming thickness is a common approximation made when modeling thermal pressurization [*Rempel and Rice*, 2006; *Noda et al.*, 2009; *Garagash*, 2012]. This approximation forces us to choose where in the deforming zone we want to evaluate the fault strength. We choose to use the pore pressure at the center of the deforming zone, $p_{\mathrm{mp}} = p_{y=0}$, which leads to

$$\tau_f = f\left(\sigma_n - p_{\mathrm{mp}}\right). \tag{11}$$

The parameter p_{mp} is almost always equal to the peak pore pressure within the deforming zone and thus the location with the lowest strength. Although the assumptions in this paragraph are severe, they are currently the only way to avoid the complicated process of modeling the evolution of strain rate localization within the gouge for every point on the fault during rupture propagation.

When thermal decomposition is accounted for it is possible that the pore pressure will become equal to—or even exceed—the normal stress. This is in contrast with thermal pressurization alone where the pore pressure is always less than the normal stress, provided that the normal stress does not experience large changes during rupture. Currently, it is not clear what happens when the pore pressure reaches the normal stress, though it may be possible for the fault to slide at zero shear strength for some period of time. Another possibility studied in *Brantut and Rice* [2011] is that the excess pore fluid pressure leads to fault opening, and this dilatancy returns the pore pressure to a value less than or equal to the normal stress. Due to the uncertainty in mechanical response we will assume throughout this paper that any simulation that leads to $p \geq \sigma_n$ is unphysical. Any simulations with back slip (i.e., $V < 0$) are also unphysical, because frictional resistance must act in the direction opposite to the direction of the slip rate.

2.4. Elastodynamics for a Steady Slip Pulse

In this subsection we show how the along-fault shear strength profile combines with the background stress driving the rupture to control the along-fault slip rate profile. We model a slip pulse with length L traveling at a constant rupture velocity v_r on a one-dimensional fault driven by a background stress τ_b. The half spaces on either side of the fault have a shear modulus μ and shear wave speed c_s. For this geometry and a subsonic rupture velocity the stress on the fault is related to the slip rate profile through the integral equation [*Weertman*, 1980]

$$\tau(x) = \tau_b - \frac{\bar{\mu}}{2\pi v_r} \int_0^L \frac{V(\xi)}{x - \xi} \mathrm{d}\xi \quad , \quad V(x) = v_r \frac{\partial \delta}{\partial x}. \tag{12}$$

Here $\bar{\mu} = \mu F(v_r/c_s)$ is the apparent shear modulus, and F decreases as the rupture velocity increases. We will model a mode III rupture, for which $F = \sqrt{1 - (v_r/c_s)^2}$, though our work could be recast in the form of a mode II rupture using the expression for F given in *Rice et al.* [2005].

To determine where on the fault slip occurs we compare the fault strength τ_f from equation (11) with the stress on the fault τ given by equation (12). Slip occurs when the stress is equal to the strength, allowing us to write

$$\tau = \tau_f \quad , \quad V > 0 \quad , \quad x \in (0, L), \tag{13}$$

$$\tau < \tau_f \quad , \quad V = 0 \quad , \quad x \notin (0, L). \tag{14}$$

As shown by *Garagash* [2012] we can determine if these conditions are satisfied using the stress rate intensity factor at the trailing edge of the slip pulse

$$k_L = -\frac{4}{\pi\sqrt{L}} \int_0^L \sqrt{\frac{x}{L-x}} \frac{\mathrm{d}\tau}{\mathrm{d}x} \mathrm{d}x. \tag{15}$$

If $k_L > 0$, then the rate of stress rebound immediately behind the slip pulse is infinite, leading to a stress that exceeds the strength in the locked portion of the fault. If $k_L < 0$ then back slip occurs immediately ahead of the trailing edge of the pulse. Thus, a slip pulse is only self-healing if $k_L = 0$.

3. Parameter Values

In this section we discuss the parameters used in this paper. The hydraulic parameters α_{hy} and Λ are poorly constrained and will vary with pore pressure, temperature, and amount of damage to the gouge material. For the Green's function solution used in this paper we must assume constant hydraulic properties, but we account for changes in the hydraulic properties with pressure and temperature using the path-averaged parameters modeling a damaged material from *Rempel and Rice* [2006]. This parameter set is based on the data in Tables 1–3 from *Rice* [2006] and uses the procedures in *Rice* [2006] to account for variations in the hydraulic properties due to damage as well as pore pressure and temperature changes. This leads to $\alpha_{\mathrm{hy}} = 6.71$ mm^2/s and $\Lambda = 0.3$ MPa/K.

The thermal parameters α_{th} and ρc are much more tightly constrained than the hydraulic parameters. Again, we follow *Rempel and Rice* [2006] and choose the specific heat capacity $\rho c = 2.7$ MPa/K and thermal diffusivity $\alpha_{\mathrm{th}} = 0.54$ mm^2/s. Both of these fall in the typical range of values quoted in *Rice* [2006].

Throughout this paper we model the decarbonation of calcite

$$\mathrm{CaCO_3} \rightarrow \mathrm{CaO} + \mathrm{CO_2} \tag{16}$$

To model this reaction we use the kinetic parameters from *Dollimore et al.* [1996] and the values of E_r and P_r given in *Platt et al.* [2015]. Our choices are $A = 2.95 \times 10^{15}$ 1/s, $Q = 319$ kJ/mol, $E_r = 3060$°C, and $P_r = 7.42$ GPa, and a more detailed discussion of these parameter choices can be found in *Sulem et al.* [2009] and *Platt et al.* [2015]. All simulations in this paper are performed for an initial reactant mass fraction $\bar{m} = 0.5$, which is large enough to make reactant depletion negligible. For other reactions with lower values of E_r reactant depletion may become important even at high initial reactant mass fractions.

To model the ambient state of the gouge before slip begins we assume an effective stress gradient of 18 MPa/km and a geotherm of 30°C/km. The majority of calculations are done for a depth of 10 km, which corresponds to an ambient effective stress $\bar{\sigma}_a = 180$ MPa and an ambient temperature of 300°C. This is slightly deeper than the depth of 7 km modeled by the parameter set from *Rempel and Rice* [2006], and this depth was chosen to ensure that thermal decomposition is triggered over a broad range of background stresses.

All solutions in this paper are performed with a friction coefficient of $f = 0.6$, a value chosen to agree with low strain rate deformation governed by Byerlee's law. Following *Garagash* [2012] we choose $\mu = 30$ GPa and $c_s = 3$ km/s. Combining these with the parameter choices above, we use the formula for a characteristic rupture velocity given in *Garagash* [2012]

$$v^* = \frac{\mu}{\tau_0} \frac{\delta_c}{T^*} = \frac{\mu}{\tau_0} \frac{\rho c}{f\Lambda} \frac{4\alpha}{W} \tag{17}$$

where $\tau_0 = f(\sigma_n - p_a)$ is the initial shear strength of the gouge, $\delta_c = \rho c W/(f\Lambda)$ is the slip-weakening distance for thermal pressurization alone, $\alpha = (\sqrt{\alpha_{th}} + \sqrt{\alpha_{hy}})^2$ is a lumped hydrothermal diffusivity, and $T^* = W^2/(4\alpha)$ is

Table 1. Table Outlining the Base Parameter Choices Used in Our Simulations[a]

Parameters	Units	Values
α_{th}	mm^2/s	0.54
ρc	MPa/K	2.7
Λ	MPa/K	0.3
α_{hy}	mm^2/s	6.71
E_r	°C	3060
P_r	GPa	7.42
$\tilde{m}$		0.5
A	1/s	2.95×10^{15}
Q	kJ/mol	319
R	J/(K mol)	8.31
W	μm	250
β		2
f		0.6
$\sigma_n - p_a$	MPa	180
θ_a	°C	300
v^*	m/s	737

[a]The thermal and hydraulic parameters are taken from *Rempel and Rice* [2006] and are based on the data in Tables 1–3 from *Rice* [2006] and the procedures in *Rice* [2006] used to account for variations due to damage, pore pressure, and temperature changes. The reaction parameters for decarbonation of calcite are taken from *Sulem et al.* [2009], but we got the notation for E_r and P_r from *Platt et al.* [2015]. The mechanical parameters follow the choices made in *Garagash* [2012]. Finally, the ambient conditions model a depth of 10 km assuming an effective stress gradient of 18 MPa/km and a geotherm of 30°C/km.

the timescale for hydrothermal diffusion to relieve pore pressures in the deforming zone. For these parameter choices we find $v^* = 737$ m/s.

Finally, we choose the parameters describing the thickness of the deforming and reacting zones. We choose the deforming zone thickness $W = 250$ μm, which is in reasonable agreement with laboratory and field observations showing micron-scale localization as well as theoretical predictions for localized zone thicknesses for strain localization driven by thermal pressurization and thermal decomposition [*Rice et al.*, 2014; *Platt et al.*, 2014, 2015]. Appendix C uses finite difference simulations that make no assumptions about the reacting zone shape to validate our approximation of the reacting zone. Based on these results, we choose $\beta = 2$, which makes the reacting zone half the width of the deforming zone.

The parameters listed above are summarized in Table 1. These are not definitive values and strong arguments could be made for quite different values for some of the parameters. We will perform additional simulations that study the dependence on different key parameters, allowing our results to be reinterpreted for a much wider range of parameter choices than specified in this section. While the model presented in the previous section has many parameters, as shown in Appendix A, the solution is controlled by seven dimensionless parameters. This reduces the number of parameter sweeps that must be performed to explore the behavior of the model.

4. The Signature of Thermal Decomposition

In this section we solve for self-healing slip pulses using the parameters in Table 1. To find self-healing slip pulses we use the numerical methods outlined in Appendix B to solve for a slip pulse with an imposed slip duration T_{pulse}, allowing us to determine the stress rate intensity factor at the trailing edge of the pulse k_L as a function of the ratio of the slip duration and the timescale for hydrothermal diffusion to drain the gouge layer T_{pulse}/T^*. Figure 2 shows the results of these simulations, alongside the solutions for thermal

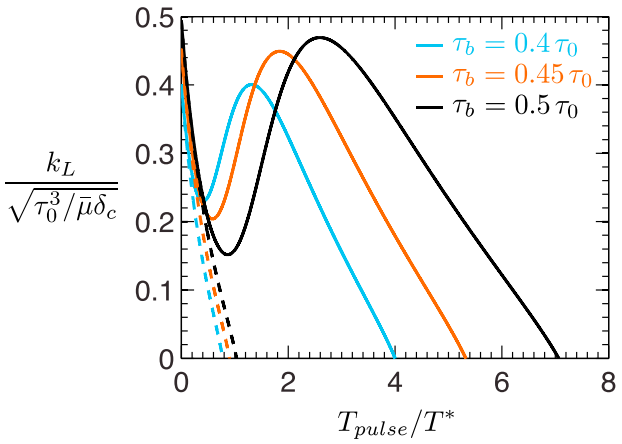

Figure 2. A plot showing how the stress rate intensity factor k_L at the trailing edge of the slip pulse varies with slip duration for three different background stresses when thermal decomposition is accounted for (solid lines), alongside the corresponding solutions for thermal pressurization alone (dashed lines). For short slip durations the solutions with and without thermal decomposition agree closely, but as the slip duration increases, thermal decomposition contributes more to the overall dynamic weakening and k_L rises above the values found for thermal pressurization alone. For the three background stresses shown here we find self-healing slip pulses, where $k_L = 0$, that trigger thermal decomposition and have slip durations many times higher than expected for thermal pressurization alone. Qualitatively extrapolating to higher background stresses we predict that there will be a range of background stress where multiple self-healing slip pulses exist, corresponding to multiple intercepts with the line $k_L = 0$.

pressurization alone from *Garagash* [2012], for three different ratios of the background stress τ_b and the initial shear strength of the gouge layer τ_0. Initially, the curves with and without thermal decomposition agree, as the total slip accommodated across the slip pulses is not high enough to trigger thermal decomposition for the lowest values of T_{pulse}/T^*. However, the total slip in the pulse rises with T_{pulse} and thermal decomposition is eventually triggered, leading to values of k_L above those obtained for thermal pressurization alone. Eventually, hydrothermal diffusion causes k_L to decrease to zero and we find self-healing slip pulses driven by thermal decomposition at longer slip durations than for thermal pressurization alone. Figure 2 is the only plot in this paper that shows slip pulses that do not satisfy the self-healing condition $k_L = 0$. Henceforth, all results contain only self-healing slip pulses, and the slip duration of a self-healing slip pulse is defined as T_{sh}.

All three curves in Figure 2 have a triple-valued shape reminiscent of a cubic curve. Extrapolating the curves in Figure 2 to higher background stress we expect three distinct self-healing slip pulses to exist for a finite range of τ_b. To find these distinct solutions we include the self-healing condition $k_L = 0$ in the Newton-Raphson iteration instead of finding solutions satisfying $k_L = 0$ by varying T_{pulse}. As expected, multiple solutions exist for a finite range of τ_b, and these solutions are described in detail below.

4.1. Slip Rate Evolution

Figure 3 shows the along-fault slip rate profiles for three distinct solutions found using the parameters in Table 1 and the background stress $\tau_b = 0.68\tau_0$. The specific value of τ_b has no special significance apart from being a value for which three distinct solutions exist. All three solutions show peak slip rates on the order of a few meters per second, and the peak slip rate decreases as the slip duration increases. Note that the three solutions show quite different slip rate profiles. The short duration solution has peak slip rates near the tip followed by a gradual decay as the trailing edge of the rupture approaches; the intermediate duration solution has a similar shape to the short duration solution with a small increase in the derivative of V with respect to x near the trailing edge of the pulse; the long-duration solution looks very different from the other two solutions with peak slip rates occurring near the trailing edge of the slip pulses at the onset of thermal decomposition. Below we will show that the three solutions correspond to different balances between thermal pressurization and thermal decomposition. The change in slope observed in the intermediate-duration solution and the peak slip rate near the trailing edge of the long-duration solution are associated with the onset of thermal decomposition.

4.2. Temperature Evolution

Figure 3 shows the temperature in the center of the deforming zone for the short-, intermediate-, and long-duration solutions. The solid curves show the temperature evolution while the fault is slipping, and the dashed curves show how the temperature falls after the fault locks. These results were generated using the parameters in Table 1 and the background stress $\tau_b = 0.68\tau_0$. We observe that the short-duration solution has a significantly lower peak temperature than the other two solutions. Despite the different slip rate profiles—leading to distinctly different frictional heating—the intermediate- and long-duration solutions have comparable peak temperatures of 847°C and 871°C.

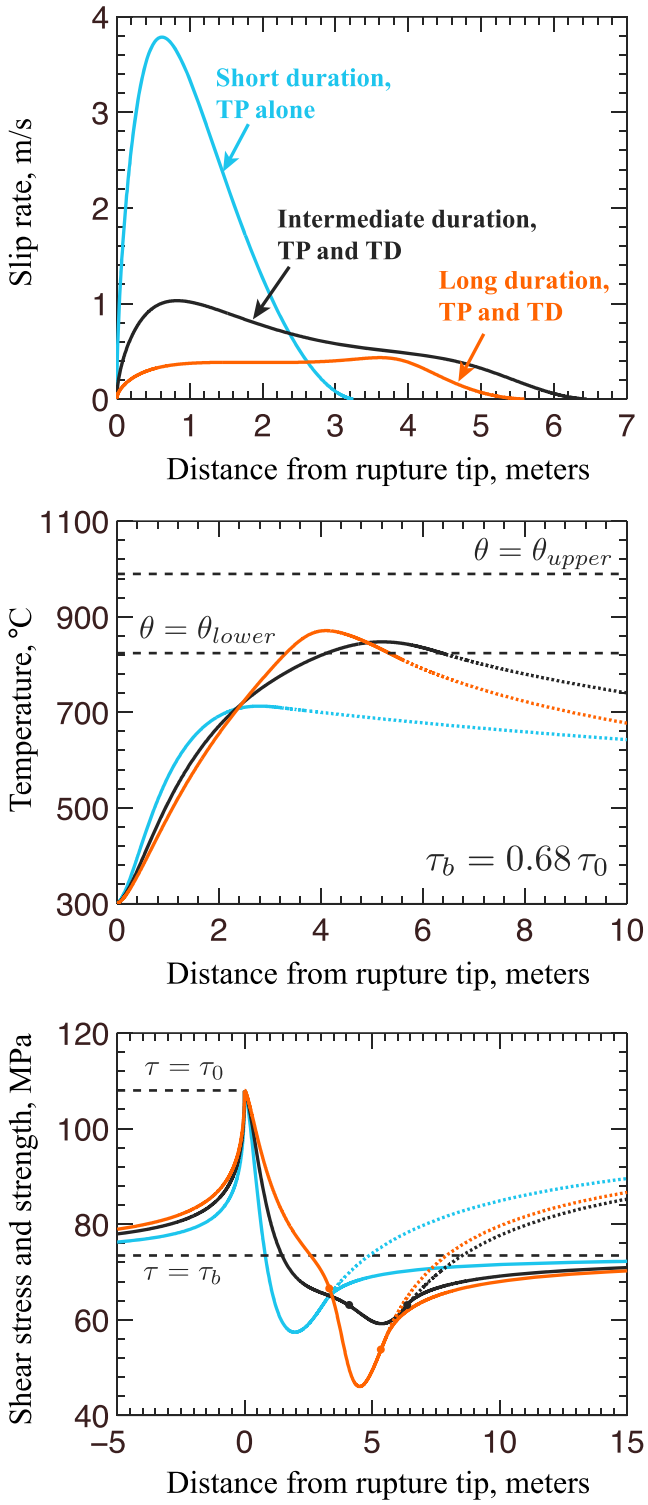

Figure 3. A plot showing the slip rate, temperature, and shear stress and strength profiles for the three self-healing slip pulse solutions found using the parameters in Table 1 and a background stress of $\tau_b = 0.68\tau_0$. In the temperature plot the dotted lines indicate the temperature evolution of the fault after slip ceases. In the shear stress plot the dotted lines show how the strength evolves after slip ceases. The blue, black, and red curves show the short, intermediate, and long-duration slip pulses, respectively. The short slip duration solution experiences weakening due to thermal pressurization alone, while the intermediate and long slip duration solutions both trigger thermal decomposition. We plot our estimates for θ_{lower} and θ_{upper} alongside the temperature curves and use dots to indicate the points at which $\theta = \theta_{\text{lower}}$ on the stress curves.

We can estimate the temperature that must be attained before thermal decomposition provides significant weakening by comparing the rate at which thermal decomposition decreases the shear strength with the rate at which hydraulic diffusion increases the shear strength. When these two processes exactly balance

$$-\alpha_{\mathrm{hy}} \left.\frac{\partial^2 p}{\partial y^2}\right|_{y=0} = \bar{m}\left(P_r - \Lambda E_r\right) A \exp\left(-\frac{Q}{R\theta_{\mathrm{mp}}}\right). \tag{18}$$

During the bulk of the slip pulse the shear stress is comparable to the background stress, and thus, the pore pressure in the center of the gouge layer is roughly equal to $\sigma_n - \tau_b/f$. Approximating the second derivative of p by combining the difference between the pore pressure in the center of the gouge layer and the ambient pore pressure with the deforming zone thickness, we arrive at

$$\alpha_{\mathrm{hy}} \frac{\tau_0 - \tau_b}{fW^2} = \bar{m}\left(P_r - \Lambda E_r\right) A \exp\left(-\frac{Q}{R\theta_{\mathrm{mp}}}\right). \tag{19}$$

Rearranging this, we find an estimate for the temperature above which thermal decomposition can overcome hydraulic diffusion

$$\theta_{\mathrm{lower}} = \frac{Q}{R}\left[\log\left(\frac{\bar{m}(P_r - \Lambda E_r)AfW^2}{\alpha_{\mathrm{hy}}(\tau_0 - \tau_b)}\right)\right]^{-1}. \tag{20}$$

Using similar arguments we can predict an upper bound on the temperature during the slip pulse by comparing the rate at which frictional heating increases temperature with the rate at which the endothermic reaction decreases temperature. When these two processes exactly balance

$$\frac{\tau V}{\rho c W} = \bar{m} E_r A \exp\left(-\frac{Q}{R\theta_{\mathrm{mp}}}\right). \tag{21}$$

As before we approximate the shear stress using τ_b and assume that the slip rate scales as δ_c/T^*, leading to

$$\theta_{\mathrm{upper}} = \frac{Q}{R}\left[\log\left(\frac{\bar{m}E_r A\rho c T^* W}{\tau_b \delta_c}\right)\right]^{-1}. \tag{22}$$

The parameter θ_{upper} should act as an upper bound on the temperature during a slip pulse because when $\theta = \theta_{\mathrm{upper}}$ the endothermic reaction totally offsets frictional heating, and thus the time derivative of θ must be negative.

Figure 3 shows how the two estimates θ_{lower} and θ_{upper} compare with the peak temperatures for the short-, intermediate-, and long-duration solutions. As expected the peak temperature in the short-duration solution is lower than θ_{lower}, indicating that thermal decomposition provides negligible dynamic weakening and this solution is equivalent to that found in *Garagash* [2012] for thermal pressurization alone. The intermediate- and long-duration solutions both exceed θ_{lower} near the trailing edge of the slip pulse, but the temperature drops below θ_{lower} just before healing occurs. As expected, both solutions that trigger thermal decomposition have peak temperatures far below θ_{upper}.

The temperature curves can be combined with equation (2) to test our assumption that reactant depletion is unimportant. We find that the final reaction extent $\Delta\xi$ at the cessation of slip is negligible ($< 0.01\%$) for the low-duration solution, 1.2% for the intermediate-duration solution, and 4.5% for the long duration solution. These low values of $\Delta\xi$ validate our assumption that reactant depletion is negligible for the decarbonation reaction studied here. Multiplying the final reaction extent by $\bar{m}E_r$, we can also find the total temperature rise offset by the reaction for each solution, finding 45°C for the intermediate-duration solution and 168°C for the long-duration solution. This suggests that reactant depletion may be important for the dehydration reactions from *Platt et al.* [2015], which typically have lower values of E_r comparable to the values for total temperature rise offset listed above.

4.3. Stress and Strength Evolution

In this subsection we investigate the along-fault stress and strength profiles for the three solutions, as shown in Figure 3 for the parameters in Table 1 and the background stress $\tau_b = 0.68\tau_0$. The solid lines show the stress for each solution and the dashed lines show the strength. The behavior for both stress and strength can be

easily understood in physical terms. Ahead of the slip pulse the strength is equal to the initial value τ_0, during slip the strength is equal to the stress and we see dramatic weakening due to thermal pressurization and decomposition, and far behind the slip pulse the strength returns to the initial strength due to hydrothermal diffusion. Far ahead of the slip pulse the stress is equal to the background stress τ_b but rises to the initial strength τ_0 as the stress concentration at the rupture tip approaches. During slip the stress is equal to the strength, and behind the slip pulse the stress rebounds to the background stress. For the intermediate- and long-duration solutions we plot the locations at which the temperature crosses θ_{lower} on the stress curves using solid circles, demonstrating that the acceleration in the weakening rate corresponds to the onset of thermal decomposition. Note that even for solutions that trigger thermal decomposition, at any given instant the majority of the slipping patch weakens through thermal pressurization alone.

To quantify the total dynamic weakening due to thermal pressurization and thermal decomposition, and total strengthening provided by hydrothermal diffusion, we integrate the first, second, and third terms on the right-hand side of equation (7) across the slip pulse. We find the total pore pressure rise due to thermal pressurization to be $\Lambda\Delta T$, where ΔT is the difference between the ambient and final temperature in the slip pulse, and the total pore pressure rise due to thermal decomposition $\bar{m}P_f\Delta\xi$, and the pore pressure drop from hydrothermal diffusion. The total weakening due to thermal pressurization is 123 MPa, 156 MPa, and 153 MPa for the short-, intermediate-, and long-duration solutions, respectively. The total weakening due to thermal decomposition is 45 MPa and 168 MPa for the intermediate- and long duration solutions, respectively. From this we conclude that the three different solutions correspond to different balances between thermal pressurization and thermal decomposition, with the long-duration solution being most affected by thermal decomposition and the short-duration solution being unaffected by thermal decomposition. Note that thermal pressurization provides a significant amount of weakening in all three solutions. Finally, we calculate the total restrengthening from hydrothermal diffusion during slip, finding pore pressure rises of 50 MPa, 127 MPa, and 236 MPa for the low-, intermediate-, and long-duration solutions, respectively. As expected the total restrengthening provided by hydrothermal diffusion increases with the slip duration.

Our results show that small changes in peak temperature can lead to large changes in total weakening due to thermal decomposition. We can understand this sensitive dependence using the reaction kinetic given in equation (2), which shows that the reaction rate increases by roughly an order of magnitude every 75°C for temperatures between 700°C and 1000°C.

4.4. Bulk Rupture Properties

In this subsection we study how the bulk rupture properties vary with background stress. Figure 4 shows how the slip duration, slip pulse length, total slip, and rupture velocity vary as a function of τ_b/τ_0 for the parameters in Table 1. For the highest values of τ_b we see that the solutions accounting for thermal decomposition (solid lines) are the same as the solutions that consider thermal pressurization alone (dashed lines). This is because the total slip at these background stresses is insufficient to raise the fault temperature to a point where the reaction is activated. As the background stress decreases we eventually see thermal decomposition become important. For a finite range of τ_b three solutions exist, with the distinctive characteristics of each solution described in the previous subsections, and beneath a critical background stress a unique solution exists that always triggers thermal decomposition. We see that thermal decomposition leads to longer slip durations, as was shown in Figure 2, and a slip pulse length that is larger than the value for solutions that consider thermal pressurization alone. The dependence of slip pulse length on background stress when thermal decomposition first becomes important is complicated, with a loop formed in the region where multiple solutions exist. When multiple solutions exist we see that the longer slip duration solutions also accommodate a larger total slip, though the difference in slips between the three solutions is at most a factor of 2. We see that the rupture velocity decreases as the total contribution of thermal decomposition increases, and almost all rupture velocities are a significant fraction of the shear wave speed.

One striking feature in Figure 4 is the close agreement of the solutions that account for thermal decomposition and the solutions for thermal pressurization alone as $\tau_b \to 0$, with this being especially notable for the plot showing total slip. Calculating the total pore pressure rise due to thermal pressurization and thermal decomposition as a function of background stress shows that thermal pressurization dominates as the background stress approaches zero, with thermal decomposition providing only a small amount of extra weakening far back from the rupture tip. This additional weakening leads to a slightly longer rupture duration and slip pulse length due to the additional time taken for hydrothermal diffusion to overcome the additional weakening

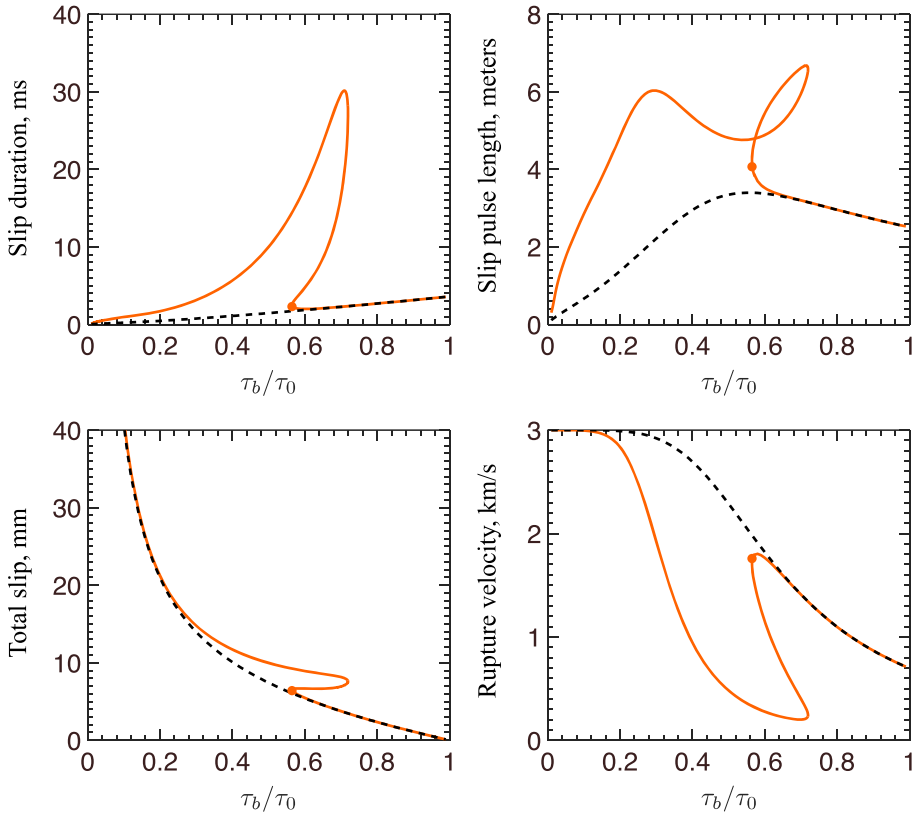

Figure 4. A plot showing how the slip duration, slip pulse length, total slip, and rupture velocity vary with background stress for the parameters in Table 1 (solid lines), alongside the corresponding curves for thermal pressurization alone (dashed lines). We see that at high background stresses the temperature rise is not large enough to trigger thermal decomposition, and for intermediate background stresses multiple solutions exist, corresponding to different balances between thermal pressurization and thermal decomposition. We indicate the point at which the peak temperature in the pulse equals θ_{lower} using dots and see that this nicely separates the solutions which trigger thermal decomposition from the solutions that experience thermal pressurization alone. At all background stresses thermal decomposition is associated with larger values of slip duration, slip pulse length and total slip, and smaller rupture velocities when compared with slip pulses driven by thermal pressurization alone.

from thermal decomposition and heal the fault. We believe that the agreement between the two solutions is partly a coincidence due to our parameter choices, which led to a maximum temperature rise when thermal decomposition is active that is very similar to the maximum temperature rise for the thermal pressurization alone solutions as $\tau_b \to 0$. We tried to test the behavior as $\tau_b \to 0$ for different parameter sets that trigger thermal decomposition more vigorously—for example, lowering the activation energy of the reaction Q—but found that this always led to pore pressures that exceed the normal stress, which is a situation we consider unphysical. We found that for $0 < \tau_b < 0.4$ the peak slip rate always occurs near the tip, and the slip rate profiles of all slip pulses look most like the black curve in Figure 3 with peak slip rates at the tip and a small change in the slope of the slip rate curves near the trailing edge of the pulse corresponding to the onset of thermal decomposition. This observation agrees well with our conclusion that thermal pressurization provides the majority of weakening at low values of τ_b.

An explanation for the lessening effects of thermal decomposition as $\tau_b \to 0$ can be found by studying the peak temperature as a function of background stress. Figure 5 shows how the peak temperature varies with background stress for solutions accounting for thermal decomposition (blue solid line) and solutions that consider thermal pressurization alone (blue dashed line). These results were generated using the parameters in Table 1. For comparison we also plot θ_{lower} and θ_{upper} as a function of background stress. Interestingly, the peak temperature achieved during a slip pulse is insensitive to background stress when thermal decomposition is active, varying by about 15°C for background stresses in the range $0.02 < \tau_b < 0.6$. This supports

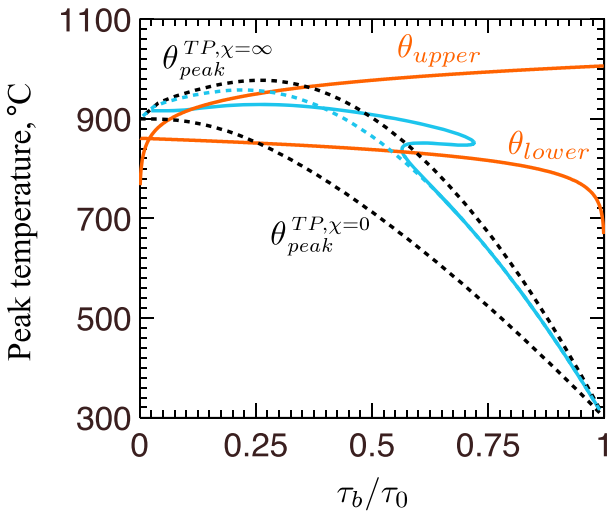

Figure 5. The solid blue curve shows how the peak temperature rise varies with background stress for the parameters in Table 1. Alongside this we plot the peak temperature rise for a slip pulse that experiences thermal pressurization alone using a blue dashed curve, and our predictions for θ_{lower} and θ_{upper} using red curves. Finally, we plot the peak temperatures for slip pulses driven by thermal pressurization alone with $\chi = \alpha_{\text{hy}}/\alpha_{\text{th}} = 0$ (undrained case) and $\chi = \infty$ (adiabatic case) using black dashed curves. Our results clearly show that the peak temperature is relatively independent of driving stress when thermal decomposition is triggered, which is consistent with an endothermic reaction that caps the temperature. Furthermore, for most values of τ_b the peak temperature rise is bounded between θ_{lower} and θ_{upper}.

the idea that the endothermic nature of the reaction sets a cap on the maximum temperature rise on a fault regardless of the amount of slip experienced.

Figure 5 also shows how θ_{lower} and θ_{upper} vary with τ_b. We observe that the point at which the peak temperature in the slip pulse intersects θ_{lower} marks the background stress below which all slip pulses trigger thermal decomposition and that all solutions with a peak temperature greater than θ_{lower} show evidence of significant weakening from thermal decomposition. This can also be observed in Figure 4, where we have plotted the location at which the peak temperature equals θ_{lower} using dots. As expected, θ_{upper} provides an upper bound on the peak temperature for all but the lowest values of τ_b, where the approximations that went into equation (22) break down because the slip rates are significantly higher than δ_c/T^*.

Finally, Figure 5 shows the peak temperature rise for thermal pressurization alone for $\chi = \alpha_{\text{hy}}/\alpha_{\text{th}} = 0$ and $\chi = \infty$. These two curves bound the temperature rise for thermal pressurization for any value of the diffusivity ratio χ. We observe that the peak temperature and the background stress at which this peak value is attained increase with χ. Since the activation of thermal decomposition relies on the peak temperature reaching θ_{lower}, the movement of the peak value of θ may explain why thermal decomposition is most pronounced for intermediate values of τ_b for the value of χ implied by the parameters in Table 1.

5. Dependence on Fault Properties

In this section we study the dependence on different parameters in the problem, with the intention of allowing our results to be reinterpreted for different reactions or parameter choices other than those made in section 3. To do this we vary different parameters in turn while fixing all other parameters at the values given in Table 1. *Garagash* [2012] showed that self-healing slip pulses driven by thermal pressurization alone are controlled by just three dimensionless parameters. These are the ratio of the hydraulic and thermal diffusivities $\chi = \alpha_{\text{hy}}/\alpha_{\text{th}}$, the ratio of the background stress to the initial strength τ_b/τ_0, and ratio of a typical rupture velocity and the shear wave speed v^*/c_s. Accounting for thermal decomposition adds four additional dimensionless parameters. The first two new dimensionless parameters R_{th} and R_{hy} control the heat absorbed and pore pressure generated by the reaction, while the other two new dimensionless parameters K and $\tilde{\theta}_a$ quantify how much the reaction rate varies with temperature and where the ambient temperature lies on a dimensionless kinetic curve. The derivation of the dimensionless set of equations and the definitions of all dimensionless parameters can be found in Appendix A.

5.1. Influence of Diffusion Timescale

First, we look at the dependence on the deforming zone thickness W, which alters the hydrothermal diffusion timescale T^* as well as the values of v^* and δ_c, which control the rupture velocity and total slip, respectively. Figure 6 shows how the bulk rupture properties vary with the background stress τ_b for four different deforming zone thicknesses varying by a factor of 8, alongside the corresponding solutions for thermal pressurization alone. As the deforming zone thickness is increased there is a tendency for the pore pressure to exceed the normal stress over a wider range of background stresses. For all plots the curves are terminated when the

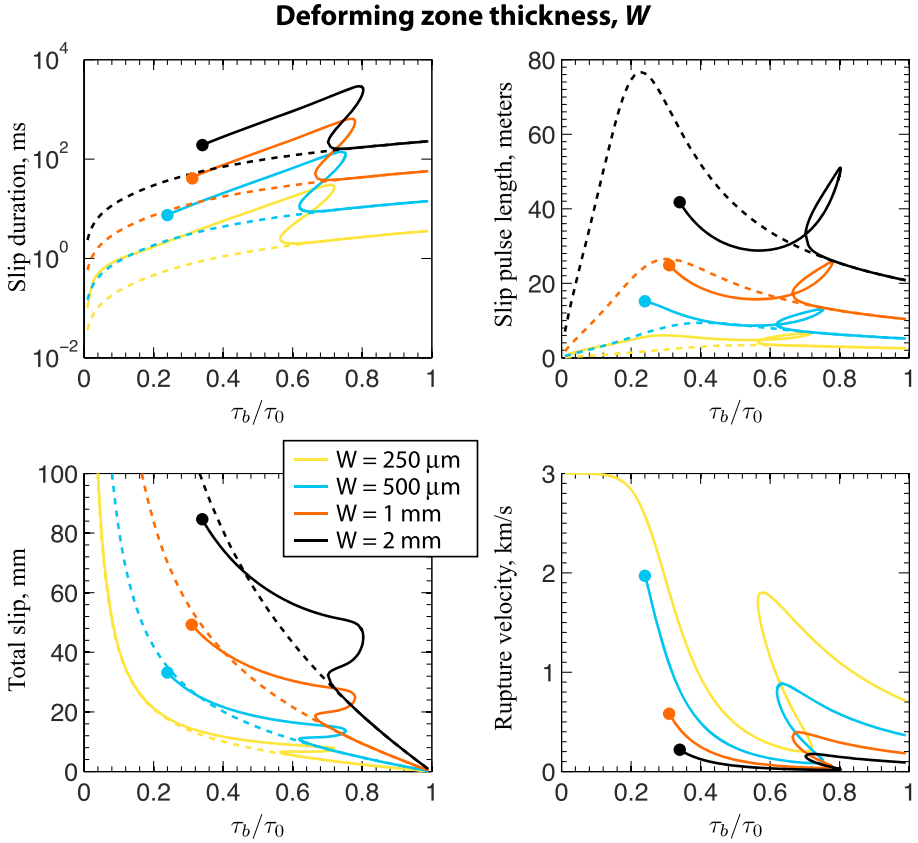

Figure 6. A plot showing how the slip duration, slip pulse length, total slip, and rupture velocity vary with background stress for four different values of the deforming zone thickness W and alongside the corresponding curves for thermal pressurization alone. The curves are terminated when the pore pressure exceeds the normal stress, and this point is noted by a circle. We see that increasing the localized zone thickness leads to larger values for slip duration, slip pulse length and total slip, and a lower rupture velocity. This is in good agreement with the results in *Garagash* [2012] that studied slip pulses driven by thermal pressurization alone.

pore pressure reaches the normal stress, and this termination is indicated by a circle. We see that T_{sh} and L increase with the deforming zone thickness but retain the same qualitative shape. The increase in slip duration is particularly large due to the quadratic dependence of T^* on W, which accounts for the majority of the change in slip duration between the different curves. Looking at the solutions in terms of the dimensionless variables, we see that the ratio T_{sh}/T^* increases by less than a factor of 2 as W increases from 100 μm to 2 mm. A similar picture is seen for total slip, with wider deforming zones leading to a larger total slip. This variation is almost entirely due to the scaling of total slip with δ_c. Finally, we see that the rupture velocity drops as the deforming zone thickness increases, and this is explained by noting that v^* decreases as $\sim 1/W$.

The behavior shown in Figure 6 is qualitatively the same as the results for thermal pressurization alone from *Garagash* [2012], which showed that as the deforming zone thickens the slip duration increases significantly and the rupture velocity drops. This is to be expected because we use the same scalings in this paper as in *Garagash* [2012].

The parameter sweep over W also allows us to see how the system will change with α and the kinetic parameter A. This is done by noting that the dimensionless parameters R_{th} and R_{hy} in Appendix A depend only on the product T^*A. However, when A is changed the scalings δ_c and v^* will remain unchanged, and when α is changed the value of δ_c remains unchanged. The dependence on the product T^*A explains why the range of background stresses with multiple solutions gradually moves to higher background stresses as W increases. In the dimensionless variables increasing W is equivalent to having a higher reaction rate constant A, which allows the reaction to be triggered at smaller slips. This equivalence with a more vigorous reaction also explains why the range of background stresses for which the pore pressure exceeds the normal stress expands as W increases.

For larger values of A the range of background stress with multiple solutions moves to higher values of τ_b. Increasing A decreases the slip duration and total slip for a fixed background stress, which can be understood by noting that a larger value of A allows the reaction to be triggered at a smaller slip but leaves the rupture velocity almost unchanged. The dependence of slip pulse length on A is complicated by the presence of multiple solutions, but in general, increasing A leads to a smaller value of L. However, the variations with A described above are much smaller than those seen in Figure 6 because changing A does not alter T^*, δ_c, or v^*, and thus we still find slip durations of a few tens of milliseconds, slip pulse lengths of few meters, total slips of a few millimeters, and rupture velocities that are a significant fraction of the shear wave speed.

Finally, as α increases, the slip duration and slip pulse length drop while the rupture velocity and total slip rise. The change in total slip is the smallest of these changes since the scaling for total slip is independent of α. The range of background stresses over which thermal decomposition is triggered also shrinks as α increases. This is to be expected in our system since increasing α decreases T^*, and this is equivalent to lowering the rate constant of the reaction A.

5.2. Balance Between Hydraulic and Thermal Diffusion

One of the striking aspects of the slip pulses driven by thermal pressurization alone presented in *Garagash* [2012] is the insensitive dependence of all rupture properties except temperature rise on the ratio of diffusivities $\chi = \alpha_{hy}/\alpha_{th}$, with the rupture properties varying by only a small amount as χ varies from 0 to ∞ while the lumped hydrothermal diffusivity α remains fixed. However, the highly nonlinear coupling between temperature and weakening produced by thermal decomposition means that this conclusion does not transfer to our model. For a fixed value of α, the lower thermal diffusivity associated with large values of χ leads to higher temperature rises, making the effects of thermal decomposition more pronounced.

Figure 7 shows how the rupture properties vary with background stress for the parameters in Table 1 and four different values of χ. As expected the signs of thermal decomposition—such as longer rupture duration—become more pronounced as χ increases. Interestingly, as χ decreases, the range of background stress over which multiple solutions exist shrinks, and for the lowest value of χ there are no values of τ_b where multiple solutions exist. Initially we thought this could occur because lowering χ was lowering the maximum temperature rise during thermal pressurization and shrinking the range of background stresses over which thermal decomposition is triggered. However, other simulations not shown here, using a rate constant two orders of magnitude greater than the value given in Table 1, show that this appears to be a feature of all simulations with values of χ comparable to or less than 1, even when thermal decomposition occurs and is important over a wide range of background stresses. This means that for low values of χ thermal pressurization is the dominant dynamic weakening mechanism. We believe this occurs because the efficient thermal diffusion associated with low values of χ makes it hard to sustain peak temperatures long enough for thermal decomposition to contribute substantial weakening.

5.3. Influence of Reaction Parameters

Next we look at the role played by the reaction parameters, beginning with the activation energy Q. Figure 8 shows how the rupture properties vary with background stress for the parameters in Table 1 and three different values of Q. We see that for a fixed background stress lowering Q does not dramatically change the rupture properties—with only a small reduction in total slip and slip pulse length—but does control the range of τ_b over which thermal decomposition is triggered. This is consistent with a reaction that adjusts so that the energy absorbed by the reaction balances the frictional heating. Lowering Q allows this balance to occur at a lower temperature, effectively moving the ambient fault conditions closer to the reaction temperature and extending thermal decomposition to higher values of τ_b. We also find that lowering Q increases the range of background stress for which the pore pressure exceeds the normal stress and increases the total pore pressure rise due to thermal decomposition during the slip pulse. These observations are both consistent with the reaction becoming more vigorous as Q decreases.

Next we look at the dependence on the temperature rise buffered by the reaction E_r and pore pressure generated by the reaction P_r, shown in Figures 9 and 10. Our results show that lowering E_r is qualitatively similar to raising P_r and that higher values of P_r lead to more distinctive features of thermal decomposition with longer slip durations, lower rupture velocities. Interestingly, the regions where the pore pressure exceeds the normal stress occur at intermediate values of τ_b for these parameter sweeps. As expected, we observe that the total pore pressure generated by thermal decomposition increases as P_r increases and drops as E_r increases.

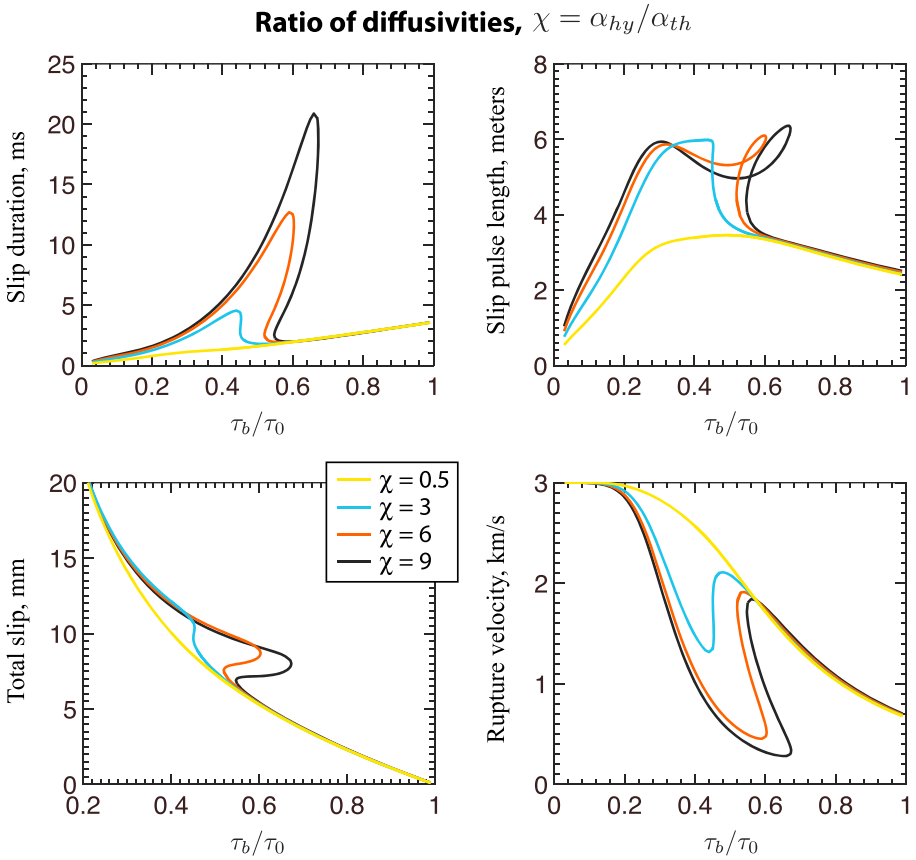

Figure 7. A plot showing how the slip duration, slip pulse length, total slip, and rupture velocity vary with background stress for four different values of the ratio between hydraulic and thermal diffusivities $\chi = \alpha_{hy}/\alpha_{th}$ and the parameters in Table 1. We observe that increasing χ leads to a more pronounced signature of thermal decomposition, with longer slip durations, larger slip pulse lengths, and lower rupture velocities. In addition, we see that for the lowest values of χ the range of τ_b for which multiple solutions exist vanishes, and the rupture properties look qualitatively similar to those for thermal pressurization alone.

The link between E_r and P_r can be motivated by studying the high-temperature limit examined in *Platt et al.* [2015] where the temperature is constant, thermal diffusion is neglected, and the reaction exactly balances frictional heating,

$$\frac{\tau\dot{\gamma}}{\rho c} = \bar{m}E_r\frac{\partial\xi}{\partial t}. \tag{23}$$

This allows us to rewrite the pore pressure equation as

$$\frac{\partial p}{\partial t} = \alpha_{\mathrm{hy}}\frac{\partial^2 p}{\partial y^2} + \frac{P_r}{E_r}\frac{\tau\dot{\gamma}}{\rho c}. \tag{24}$$

Note that this is similar to the equation for pore pressure evolution during thermal pressurization and the ratio P_r/E_r acts as an effective value of Λ. For the parameters modeling the decarbonation of calcite in Table 1, $P_r/E_r = 2.43$ MPa/K. This value is much larger than the value of Λ given in Table 1, explaining why the onset of thermal decomposition accelerates dynamic weakening. As shown in *Platt et al.* [2015], the isothermal limit described in equation (23) is likely never reached but we still advocate using the ratio P_r/E_r—which is equal to the pore pressure generated per degree of temperature rise buffered—to estimate if one thermal decomposition reaction will drive more or less weakening than another reaction. Inserting P_r/E_r in place of Λ into the formula for v^* given in equation (17) lowers the characteristic rupture velocity by almost an order of magnitude, which may partly explain why for a given background stress the slip pulses that trigger thermal decomposition always have lower rupture velocities than predicted for thermal pressurization alone.

It is important to note that the argument for E_r and P_r balancing through the ratio P_r/E_r only works when reactant depletion is negligible and that reactant depletion can be justifiably neglected when $\bar{m}E_r$ is much

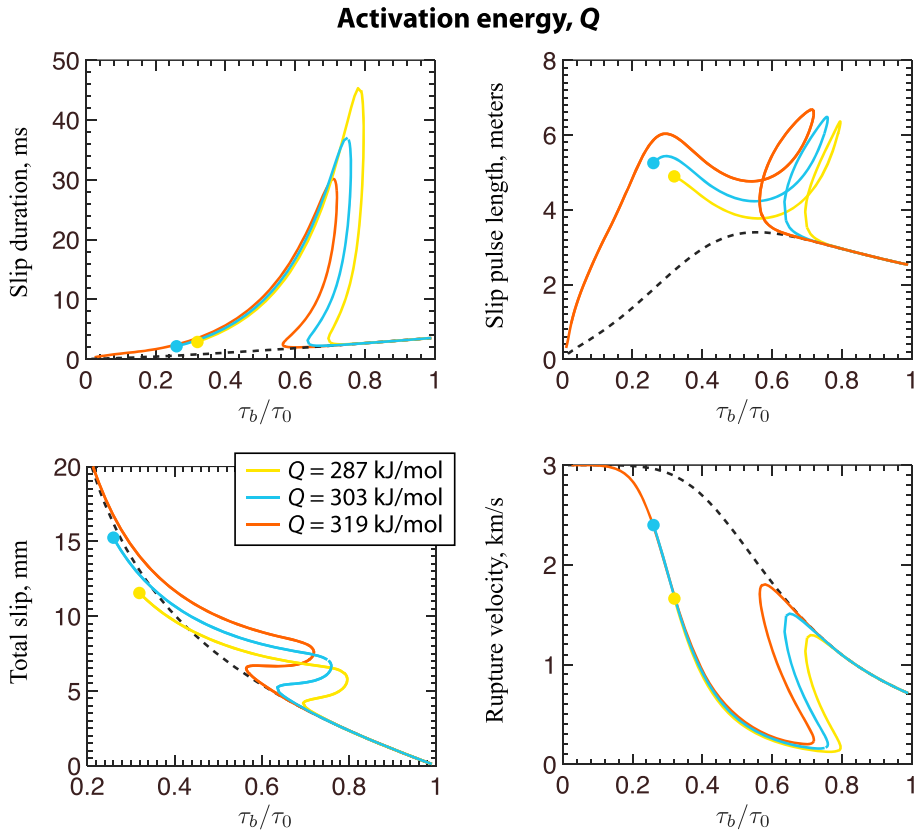

Figure 8. A plot showing how the slip duration, slip pulse length, total slip, and rupture velocity vary with background stress for three different values of the activation energy for the reaction Q and the parameters in Table 1, alongside the corresponding curves for thermal pressurization alone. The curves are terminated when the pore pressure exceeds the normal stress, and this point is noted by a circle. Lowering the activation energy makes it easier to activate thermal decomposition, leading to lower total slips and longer slip durations at high values of τ_b. Lowering Q also leads to pore pressures that exceed the normal stress over a wide range of τ_b.

larger than the total work done during slip divided by ρc. As expected, in the simulations shown in Figure 9 we observe that as E_r drops, the total reactant depletion during the slip pulses rises. When reactant depletion is important, the rate of weakening from thermal decomposition will still depend on the ratio P_r/E_r, while E_r alone controls the rate at which the reactant depletes.

5.4. Influence of Depth

Finally, we look at how the slip pulses driven by thermal decomposition depend on depth. To do this we follow the choices made in section 3 and assume a geotherm of 30°C/km and an effective stress gradient of 18 MPa/km. Figure 11 shows how the rupture properties depend on background stress for the parameters in Table 1 and depths of 10 km, 12 km, and 14 km. These three depths were selected for two reasons. First, we need to be deep enough that thermal decomposition is triggered over a wide range of background stresses. Second, we want to limit the range of background stresses for which the pore pressure exceeds the normal stress, and we found that as the depth increases the pore pressure exceeds the normal stress for a wider range of background stresses. We observe that increasing the depth extends the range of background stress for which thermal decomposition is triggered. The peak temperature achieved during the simulations shown in Figure 11 shows a modest increase with depth—varying from ~ 900°C at 10 km to ~ 975°C at 14 km—that can be explained by the increase in the heating rate $\tau\dot{\gamma}$ with ambient effective stress. The increase in heating rate also makes reactant depletion more important as the depth increases, though not enough to be important for the decarbonation reaction considered here.

Finally, we look at the balance between thermal pressurization and thermal decomposition and find that the total pore pressure rise generated by thermal decomposition normalized by the ambient effective stress increases with depth, while the pore pressure rise generated by thermal pressurization normalized by the

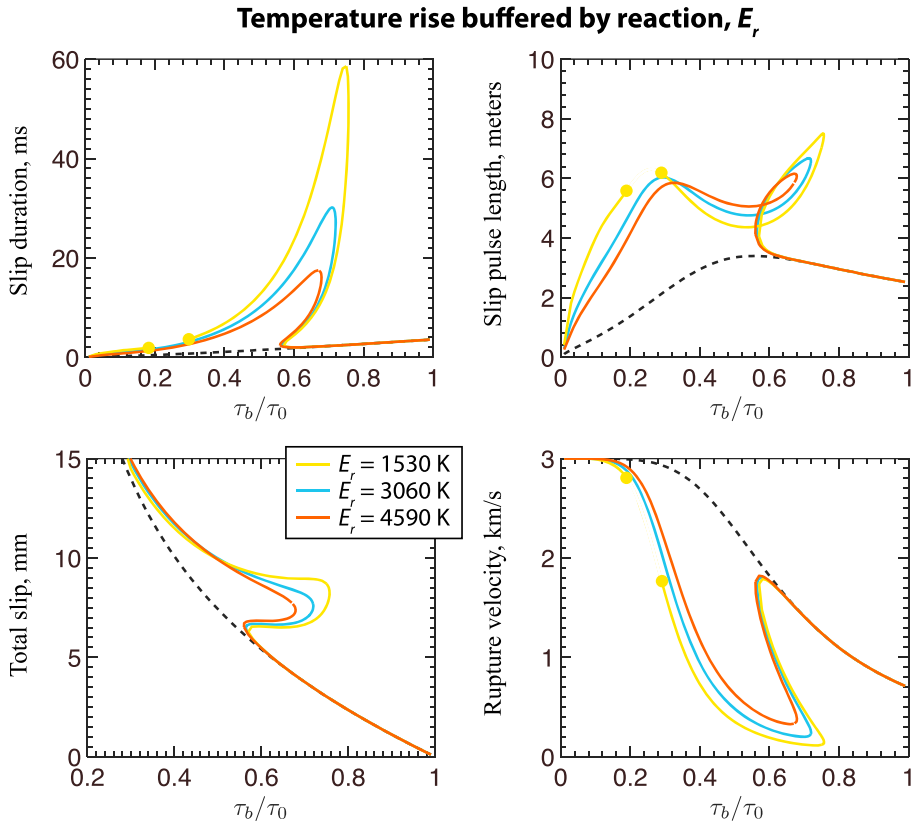

Figure 9. A plot showing how the slip duration, slip pulse length, total slip, and rupture velocity vary with background stress for three different values of E_r and the parameters in Table 1, alongside the corresponding curves for thermal pressurization alone. The curves are terminated when the pore pressure exceeds the normal stress, and this point is noted by a circle. We see that increasing E_r makes the effects of thermal decomposition less pronounced. Interestingly, the range of τ_b for which the pore pressure exceeds the normal stress occurs at intermediate values of τ_b.

ambient effective stress decreases with depth. From this we conclude that the importance of thermal decomposition as a dynamic weakening mechanism increases with depth. This may seem surprising since the dimensionless parameters R_{th} and R_{hy} decrease as $\bar{\sigma}_a$ increases. However, this can be understood by noticing that as the depth increases the reaction is triggered after a smaller slip, forcing the amount of weakening due to thermal pressurization to decrease. We believe that the increase in the contribution to total weakening from thermal decomposition is the reason that Figure 11 shows more distinctive signs of thermal decomposition as the depth increases.

6. "Trains" of Slip Pulses

When the self-healing condition $k_L = 0$ is included in the Newton-Raphson iteration, we found that some initial guesses converge to solutions with greater complexity than those shown above, which have a single local maximum in the slip rate profile. Figure 12 shows the slip rate, temperature, stress, and strength evolution for three such solutions found using the parameters in Table 1 with the deforming zone thickness set to $W = 3$ mm and a background stress $\tau_b = 0.4\tau_0$. The along-fault slip rate profile clearly shows multiple local maxima, with the number of maxima ranging from 1 to 3. An additional solution with four local maxima in the slip rate profile was also found. The along-fault profiles for temperature and stress also show multiple local maxima, and once thermal decomposition is activated the temperature is largely confined between θ_{lower} and θ_{upper}. When plotted against distance from the rupture tip the three solutions show strong overlap, suggesting that the three-peak solution is nearly equivalent to the two-peak solution with additional structure added at the trailing edge of the pulse. Since the solutions are reminiscent of a train of individual slip pulses propagating together as a coherent unit, we term these more complex solutions train-like solutions.

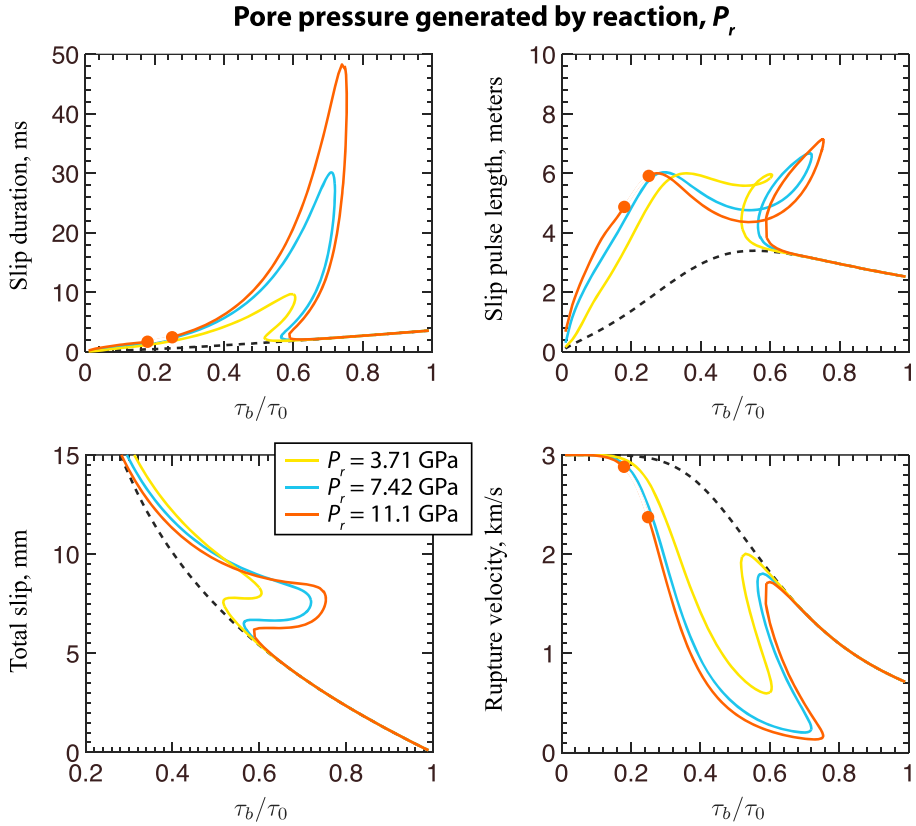

Figure 10. A plot showing how the slip duration, slip pulse length, total slip, and rupture velocity vary with background stress for three different values of P_r and the parameters in Table 1, alongside the corresponding curves for thermal pressurization alone. The curves are terminated when the pore pressure exceeds the normal stress, and this point is noted by a circle. We see that increasing P_r makes the effects of thermal decomposition more pronounced. As in Figure 9 the range of τ_b for which the pore pressure exceeds the normal stress occurs at intermediate values of τ_b.

The solutions with two and four peaks emerged naturally from initial guesses designed to find solutions with one peak, while the three-peak solution was deliberately searched for using an initial guess consisting of the first three peaks of the four-peak solution. The solutions with multiple peaks arise due to the reaction being triggered multiple times in the same slip pulse as the temperature rises and falls. The endothermic nature of the reaction and thermal diffusion combine to lower the temperature from the peak values, and frictional heating raises the temperature to the new peak. The frictional heating is aided by hydraulic diffusion raising the shear strength while the temperature falls.

Figure 13 shows how the rupture properties vary with background stress for the four train-like solutions. We see that adding more peaks to the solution increases the slip duration, slip pulse length and total slip, and reduces the rupture velocity. The more complex solutions appear to exist only for a narrow range of background stresses, with the maximum pore pressure exceeding the normal stress for lower background stresses and the slip rate becoming negative for higher background stresses. We found that the range of background stresses for which the solutions with multiple slip rate peaks exist increases as the deforming zone thickness W increases, leading to the choice of $W = 3$ mm used to find the solutions shown in Figure 12. As before we have discounted solutions with $V < 0$—suggesting that a portion of the fault is slipping in the opposite direction to the applied shear stress—as they are unphysical. The physical significance of these train-like solutions is still unclear, and we do not know if it would be possible to arrive at a propagating rupture that triggers the reaction multiple times in a time-dependent dynamic rupture model that allows for solutions that are not steady slip pulses.

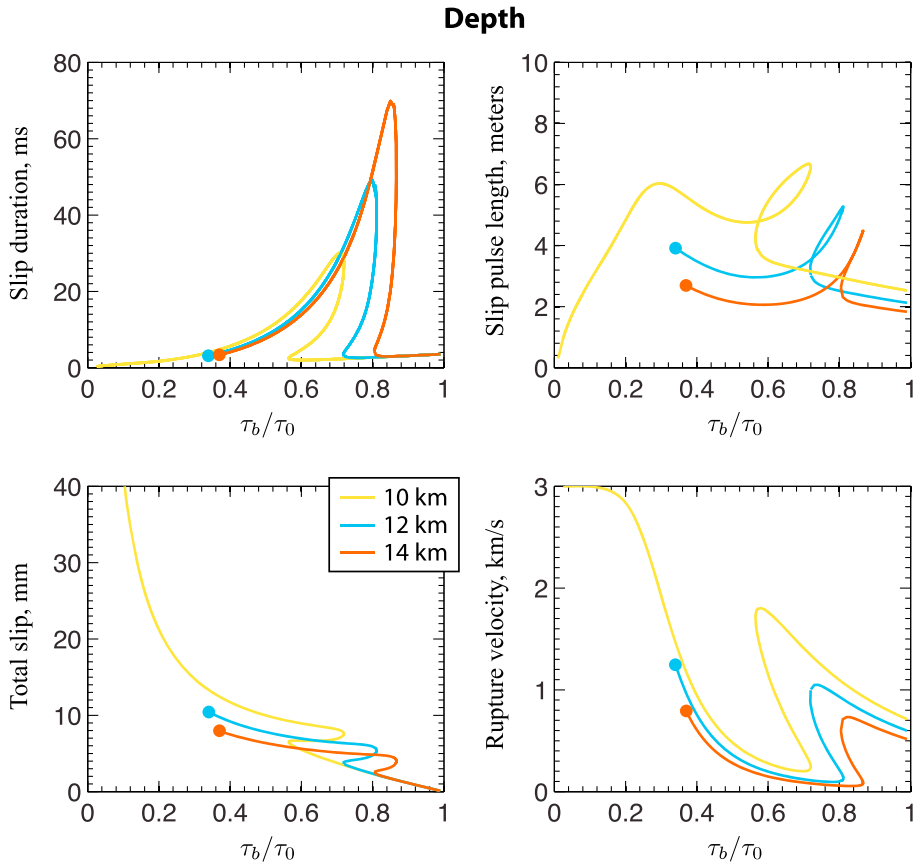

Figure 11. A plot showing how the slip duration, slip pulse length, total slip, and rupture velocity vary with background stress for three different depths and the parameters in Table 1. Here we assume the ambient fault conditions follow an effective stress gradient of 18 MPa/km and a geotherm of 30°C/km. The curves are terminated when the pore pressure exceeds the normal stress, and this point is noted by a circle. We see that the range of τ_b over which thermal decomposition is triggered expands with depth, as does the range of τ_b for which the pore pressure exceeds the normal stress. This indicates that thermal decomposition is more vigorous deeper in the seismogenic zone.

7. Discussion

7.1. Signature of Thermal Decomposition

In this paper we presented the first dynamic rupture models to account for thermal decomposition. We found that the activation of thermal decomposition leads to a distinctive along-fault slip rate profile, longer rupture durations, larger total slips, lower rupture velocities, and larger slip pulse lengths. However, some of these observations may only be true for steadily propagating self-healing slip pulses, and may not transfer to other solutions that allow for nonsteady slip pulses or crack-like ruptures. For intermediate values of τ_b—where the influence of thermal decomposition is most pronounced for steady slip pulses—the peak slip rate occurs toward the trailing edge of the pulse, coinciding with the onset of the reaction. Since, to the best of our knowledge, all other dynamic weakening mechanisms lead to peak slip rates near the rupture tip, this along-fault slip rate profile makes thermal decomposition unique.

This distinctive signature of thermal decomposition may allow it to be identified in seismic observations. While imaging details such as along-fault slip rate profile with the precision needed to determine the exact location of peak slip rate is difficult, it may be possible to see variations in slip duration, which our results suggest will change dramatically if thermal decomposition is triggered. It may also be possible to observe a seismic signature for thermal decomposition by studying the propagation of an earthquake across the equilibrium phase boundary for a reaction. For depths above the equilibrium phase boundary thermal decomposition may be an important dynamic weakening mechanism, while below the phase boundary it will produce no weakening.

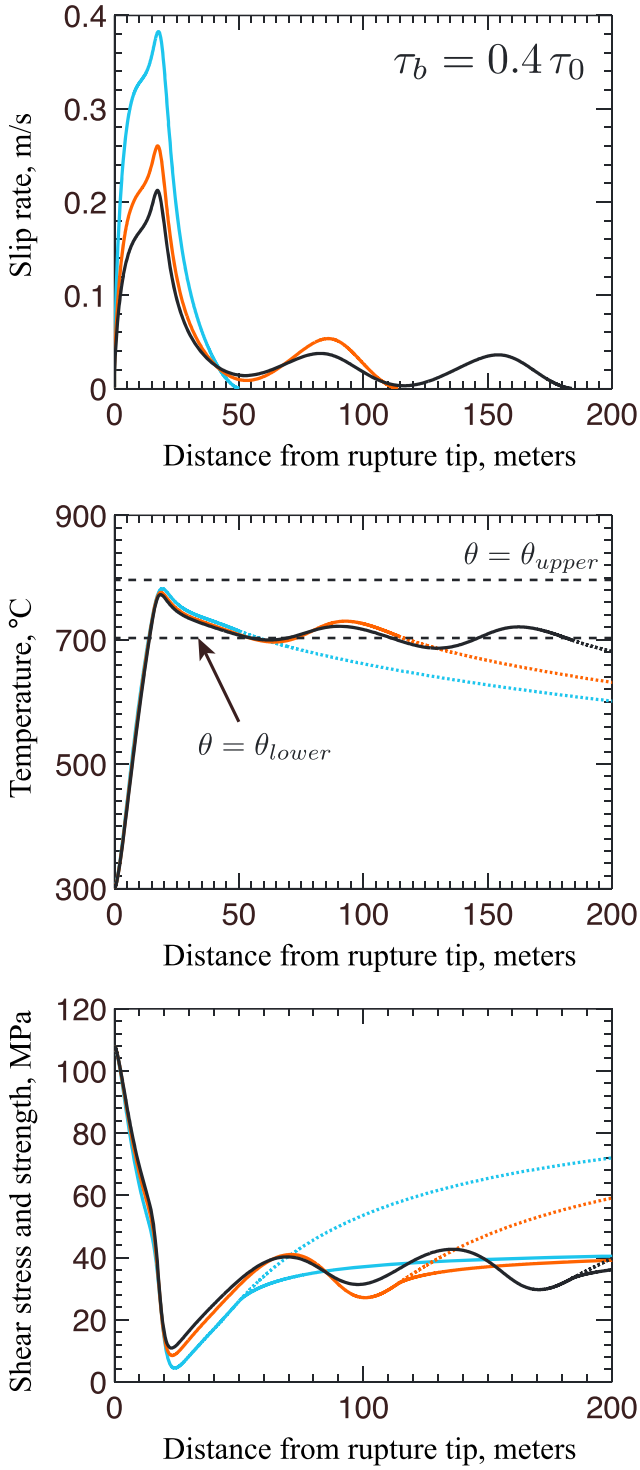

Figure 12. A plot showing the along-fault slip rate, temperature, and shear stress and strength for the solutions with multiple local maxima in slip rate. These results were produced using the parameters in Table 1, a deforming zone thickness $W = 3$ mm, and a background stress of $\tau_b = 0.4\tau_0$. In the temperature plot the dashed lines indicate the temperature evolution of the fault after slip ceases, and in the shear stress plot the dashed lines show how the strength evolves after slip ceases. Our estimates for θ_{lower} and θ_{upper} are plotted alongside the temperature curves. These solutions correspond to a single reaction being triggered multiple times within a single slip pulse. Note the similarity between the solutions, for example the two-peak solution looks similar to the first two peaks in the three-peak solution.

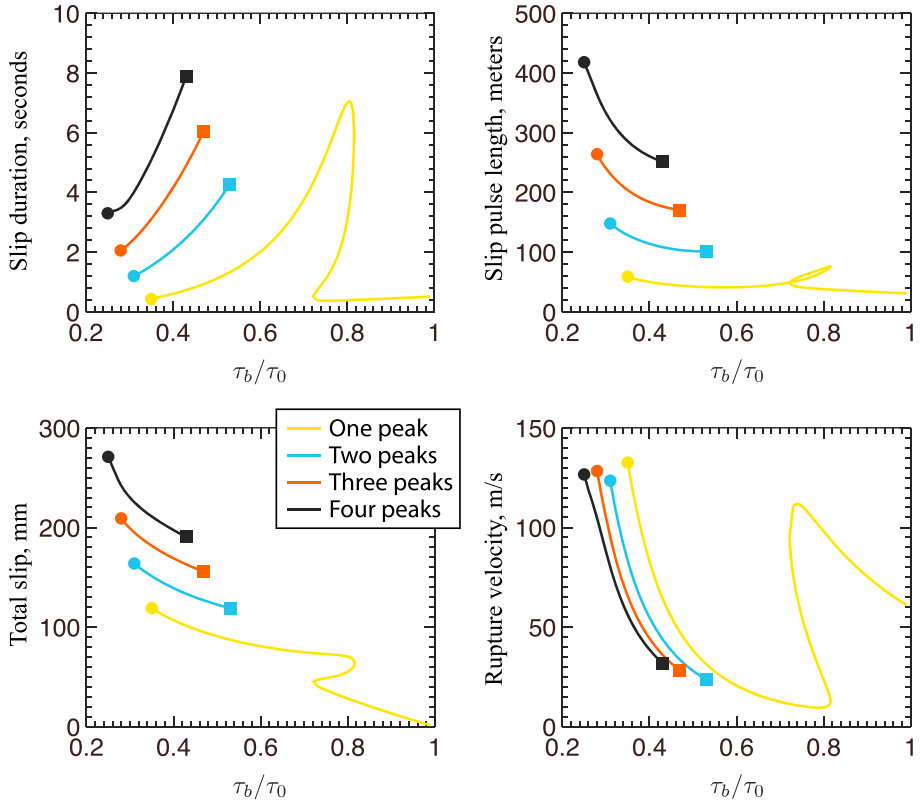

Figure 13. A plot showing how the slip duration, slip pulse length, total slip, and rupture velocity vary with background stress for the train-like slip pulses with one, two, three, and four local maxima in slip rate. These results were produced using the parameters in Table 1 and a deforming zone thickness $W = 3$ mm. The curves are terminated when the pore pressure exceeds the normal stress, which is denoted by a circle, and where the slip rate becomes negative, which is denoted by a square. We see that slip pulses with more peaks have larger slip durations, slip pulse lengths, and total slips, but the rupture velocity is comparable for all four solutions.

Our results show that the balance between thermal pressurization and thermal decomposition can change significantly with the background stress on the fault. We found that thermal decomposition is most active at intermediate background stress, though this conclusion may not be true for nonsteady slip pulses or crack-like ruptures. Regardless of this, our results definitively demonstrate that thermal decomposition can be an important dynamic weakening mechanism in a dynamically propagating rupture.

7.2. Problem of Vanishing Effective Stress

One problem we encountered frequently was the tendency for thermal decomposition to drive the pore pressure above the normal stress. Due to the uncertainty over what the mechanical response of the fault will be when the pore pressure exceeds the normal stress, we decided to consider all slip pulses with $p > \sigma_n$ unphysical. We expect this problem to occur frequently when thermal decomposition is accounted for in other more complex dynamic rupture models, and not just in our model for steady slip pulses. While preparing this paper we produced some additional solutions that accounted for the dependence of permeability on effective stress. Assuming the exponential dependence of permeability on effective stress commonly seen in laboratory measurements—for example, *Wibberley and Shimamoto* [2003]—we found that this feedback was almost always able to limit the pore pressure to values lower than the normal stress. Because the Green's function approach, used to produce the majority of the results in this paper, is not valid when the hydraulic diffusivity depends on pore pressure, these simulations were performed using the finite difference procedure outlined in Appendix C. We advocate including this dependence of permeability on effective stress in future rupture models accounting for thermal decomposition. Another similar suggestion that may limit pore pressure below the normal stress is to account for the dependence of storage capacity on effective stress when calculating P_r, which will cause P_r to decrease with the effective stress.

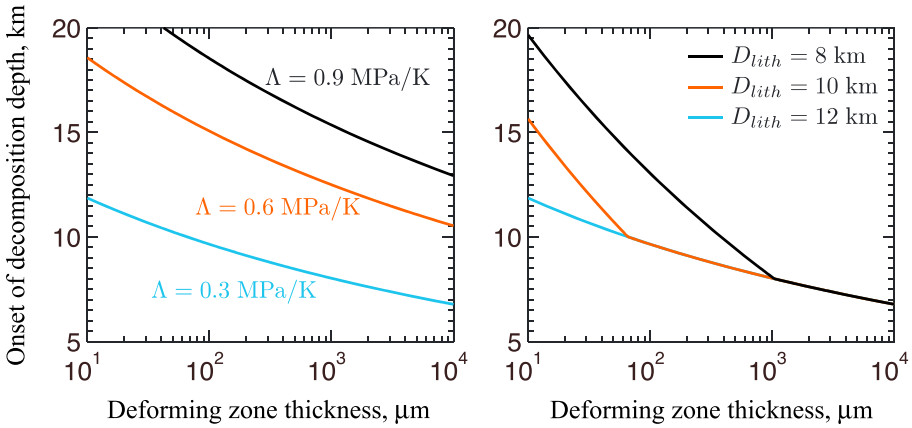

Figure 14. Two plots showing how the onset of decomposition depth varies with the deforming zone thickness for the parameters in Table 1. (left) The onset of decomposition depth increases with Λ. (right) The dependence on the depth D_{lith} at which the pore pressure gradient stops being hydrostatic and instead becomes lithostatic. Both plots can be understood by noting that the temperature rise for thermal pressurization alone scales as $\bar{\sigma}_a/\Lambda$. For both plots we see that as the deforming zone thickness increases thermal decomposition is triggered at shallower depths.

The coupling between pore pressure and permeability also produced interesting results for thermal pressurization alone and appeared to show that the initial weakening that begins at the ambient pore pressure and the restrengthening due to hydraulic diffusion that happens at higher pore pressures are governed by different values of the hydraulic diffusivity. This effect is particularly pronounced for slip pulses at low background stresses, since these slip pulses experience the largest pore pressure changes.

7.3. Onset of Decomposition Depth

In this section we extrapolate our results to predict how the depth below which thermal decomposition is triggered depends on the fault properties for an assumed geotherm of 30°C/km and an effective stress gradient of 18 MPa/km. To do this we compare our prediction for θ_{lower} given in equation (20) with the peak temperature for slip pulses driven by thermal pressurization alone and define the onset of decomposition depth to be the depth below which thermal decomposition is triggered for no value of τ_b. This is equivalent to saying that below the onset of decomposition depth, there is some value of τ_b for which thermal decomposition is triggered during a slip pulse, though this does not mean that thermal decomposition is triggered for all values of τ_b.

Figure 14 shows how the onset of decomposition depth depends on the deforming zone thickness W for different parameter choices. In Figure 14 (left) we study the dependence on the thermal pressurization coefficient Λ. As expected, we find that as Λ increases the onset of decomposition depth moves to higher values. This occurs because the peak temperature rise for thermal pressurization alone scales with $\bar{\sigma}_a/\Lambda$, so as Λ increases the peak temperature decreases, and thus, thermal decomposition is less likely to be activated. Recognizing this scaling for temperature rise motivates Figure 14 (right), which investigates how the transition from a hydrostatic pore pressure gradient to a lithostatic pore pressure gradient at a depth D_{lith} alters where decomposition is triggered. We observe that decreasing D_{lith} moves the onset of decomposition deeper into the seismogenic zone, which can be understood by noticing that decreasing D_{lith} lowers $\bar{\sigma}_a$ for all depths below D_{lith}. In both plots we observe that as the deforming zone widens, the onset of thermal decomposition moves to shallower depths. While we have only studied the dependence of the onset of decomposition depth on a few parameters, our framework could be easily extended to investigate the dependence on other parameters.

7.4. Possibility of Multiple Rupture Modes

Our results show that when thermal decomposition is accounted for there can be several different ways to propagate a steady slip pulse. To begin we showed that often, for intermediate values of τ_b, there are multiple ways to balance thermal pressurization and thermal decomposition when propagating a steady slip pulse. Following this, we showed that it is possible for a single reaction to be activated multiple times, leading to a rupture mode that looks like a train of slip pulses. We note that train-like rupture modes have been observed before in *Coker et al.* [2005], *Lapusta* [2005], *Shi et al.* [2008], and *Gabriel et al.* [2012].

Given this complexity, it is not clear how a fault would select from this range of possible rupture modes, or if a fault having ruptured once would select the same rupture mode in subsequent earthquakes. Furthermore, it is possible that a rupture switches between different modes as it propagates, possibly by only activating thermal decomposition on discrete portions of the fault. This wide range of possibilities may explain how a single fault can host earthquakes with a wide range of magnitudes. Such complexity may exist when other dynamic weakening mechanisms are coupled and our results highlight the need for thorough parameter sweeps when modeling earthquake ruptures.

If the ultimate rupture mode is selected by the manner of nucleation, then it is important to properly couple models for dynamic weakening to realistic models for nucleation. However, this will likely require significantly more code development and computational resources than were used to produce the results in this paper.

7.5. Dependence on Important Parameters

In this section we highlight the parameters that exert the greatest control over our system. To begin we discuss the dependence on the deforming zone thickness W. By studying self-healing slip pulses driven by thermal pressurization alone, *Garagash* [2012] was able to define a critical deforming zone thickness

$$h_{\text{dyna}} = \frac{\mu}{\tau_0}\frac{\rho c}{f\Lambda}\frac{4\alpha}{c_s} \tag{25}$$

and show that when the deforming zone thickness is less than or comparable to h_{dyna} the slip pulse propagates seismically, and when the deforming zone thickness is much greater than h_{dyna} the slip pulse propagates aseismically. *Garagash* [2012] also showed that the slip duration and total slip increase with the deforming zone thickness. Our simulations show that the conclusions in *Garagash* [2012] are still valid when thermal decomposition is accounted for. The majority of the change in rupture properties with W is the result of how W changes T^*, v^*, and δ_c, which scale the slip duration, rupture velocity, and total slip, respectively, allowing our results to be extrapolated to deforming zone thickness not shown here. Our results show that increasing W makes the reaction slightly more vigorous, in agreement with our observation that as the deforming zone thickness increases the range of background stress for which the maximum pore pressure exceeds the normal stress grow. We believe this increased tendency for pore pressures to exceed the normal stress occurs because it is harder for hydraulic and thermal diffusion to relieve elevated pore pressures and temperatures in a wider deforming zone.

The sensitive dependence of the rupture properties on W highlights the importance of modeling strain localization during an earthquake. *Rice et al.* [2014] and *Platt et al.* [2014] showed that thermal pressurization can drive significant strain rate localization, and *Platt et al.* [2015] showed that the onset of thermal decomposition leads to additional localization. Physical intuition suggests that if the deforming zone thins at the onset of thermal decomposition, then hydrothermal diffusion will become more efficient when the reaction is triggered, possibly offsetting a large amount of the increase in slip duration our work predicts accompanies the onset of thermal decomposition. *Rice et al.* [2014] and *Platt et al.* [2014, 2015] also showed that the localized zone thickness should evolve as the slip rate changes during a rupture. This could have interesting feedbacks with the large variations in slip rate in our slip pulse solutions, possibly slowing restrengthening due to hydraulic diffusion as the slip rate approaches zero near the trailing edge of a slip pulse.

These hypotheses could be tested by coupling the model for a self-healing slip pulse presented in this paper with the type of calculations used to model strain localization in *Rice et al.* [2014] and *Platt et al.* [2014, 2015]. However, this is complicated by the specific rate-strengthening friction law assumed by these localization models. Equation (3) from *Platt et al.* [2014] shows that the friction coefficient vanishes ahead of the slip pulse, and thus, the fault has zero strength. It may be possible to get around this by accounting for state evolution in the localization calculations. Another option may be to alter the slip pulse model to allow a small but finite slip rate to occur everywhere on the fault, instead of setting $V = 0$ for $x \notin [0, L]$. Regardless of the approach, it is likely that the Green's function formulation used to produce the results presented in this paper cannot be applied to a calculation that accounts for strain localization.

Our simulations show that the amount of weakening generated by a specific reaction is largely controlled by the ratio P_r/E_r. Increasing P_r by a factor of 2 produces results that are similar to the results found when E_r is decreased by a factor of 2. Furthermore, we presented a physical motivation for the importance of this ratio based upon the assumption that the temperature changes slowly when thermal decomposition is active. We showed that P_r/E_r plays a role similar to that played by Λ in classic models of thermal pressurization, and it is

no coincidence that the units of the ratio P_r/E_r (MPa/K) are the same as the units of Λ. Also, note that the same ratio appears in *Platt et al.* [2015] in the formula for the localized zone thickness when thermal decomposition is active and plays the same role that Λ does in the low-temperature limit dominated by thermal pressurization. An argument could be made for using $P_r - \Lambda E_r$ instead of P_r to quantify the pore pressure generated by the reaction, corresponding to a reaction that progresses under zero temperature flux conditions rather than constant temperature conditions. However, for all of the parameters used in this paper and in *Platt et al.* [2015] ΛE_r is significantly smaller than P_r, making the distinction between $P_r - \Lambda E_r$ and P_r unimportant.

It is important to note that the use of P_r/E_r to estimate the potency of a thermal decomposition is only valid when reactant depletion is negligible and that reactant depletion is controlled by the total temperature that can be buffered by the reaction $\bar{m}E_r$. Our model could easily be extended to account for reactant depletion, and this may provide another mechanism to limit the pore pressure to values lower than the normal stress. The solid volume change associated with reactant depletion may also lead to additional strengthening by increasing the hydraulic diffusivity.

Having demonstrated the importance of the ratio P_r/E_r, we can now predict which decomposition reactions will drive the most weakening. We find that all three dehydration reactions listed in *Platt et al.* [2015] (lizardite, talc, and an illite/muscovite mixture) lead to values of P_r/E_r of $\sim$ 10 MPa/K. This suggests that for these dehydration reactions thermal decomposition will be a much more efficient weakening mechanism than for the decarbonation reaction studied in this paper, for which $P_r/E_r \approx 2.4$ MPa/K. Furthermore, the values of E_r for the three dehydration reactions are $\sim$250–300°C, and thus reactant depletion may be important. These conclusions are supported by some additional self-healing slip pulse solutions we produced using the parameters from *Platt et al.* [2015] modeling the dehydration of lizardite that showed a pronounced signature of thermal decomposition and pore pressures exceeding the normal stress over a wide range of background stresses.

Another important parameter that dictates the impact of thermal decomposition is the ratio of the hydraulic and thermal diffusivities, $\chi = \alpha_{hy}/\alpha_{th}$. Figure 7 shows that the signature of thermal decomposition becomes much more pronounced as χ increases. We see that for $\chi = 0.5$ and $\chi = 3$ the range of background stresses with multiple solutions vanishes, and for $\chi = 0.5$ the results look qualitatively similar to the solutions for thermal pressurization alone. This is in stark contrast with the results for thermal pressurization alone, which showed a very modest dependence on χ. We believe χ plays such an important role by controlling the amount of time spent at the peak temperature, as well as the magnitude of the peak temperature. The efficient thermal diffusion associated with low values of χ shortens the amount of time spent at the peak temperature and thus decreases the total weakening contributed by thermal decomposition.

This dependence on χ will be important when trying to predict how the signature of thermal decomposition may be expressed at different depths in the seismogenic zone. We expect α_{hy} to fall significantly as the depth increases while α_{th} remains roughly constant. This means χ will decrease with depth and for a given reaction the signature of thermal decomposition may be most distinctive in the shallower part of the depth range where thermal decomposition is triggered.

The final parameter that plays a large role in controlling the balance between thermal pressurization and thermal decomposition is the background stress on the fault τ_b. Thermal decomposition cannot be triggered in the slip pulses found at the highest values of τ_b because the weakening provided by the reaction would be so large that healing would be impossible. In contrast, the nonsteady rupture simulations in *Noda et al.* [2009] showed that the peak temperature rise increases with background stress, suggesting that we should expect thermal decomposition to be most prevalent at the highest background stresses. Even if the steady self-healing pulse constraint is not realistic, the simulations in *Noda et al.* [2009] show that the temperature evolution of the fault changes with τ_b, and thus, the balance between thermal pressurization and thermal decomposition will change with background stress in nonsteady simulations.

7.6. Relationship Between Steady Slip Pulses and Time-Dependent Ruptures

One of the major limitations of our model is that we only solve for steadily propagating slip pulses, and it is not clear how these steady solutions relate to time-dependent ruptures that nucleate and then propagate along the fault. The dynamic rupture simulations presented in *Noda et al.* [2009] did not produce steadily propagating slip pulses, instead finding only growing slip pulses, decaying slip pulses, and crack-like ruptures. *Noda et al.* [2009] also found that the transition from decaying pulse to growing pulse occurred over a very narrow range of background stress [see *Noda et al.*, 2009, Figure 4], possibly indicating that steadily propagating slip

pulses could only exist for a very narrow range of background stress. *Gabriel et al.* [2012] studied the boundary between growing and decaying pulses in more detail for a much simpler fault strength model and managed to find pulses that propagated steadily for the entire length of the rupture simulation. *Gabriel et al.* [2012] also showed that the steady pulses form the boundary between growing and decaying slip pulses in parameter space. Both *Noda et al.* [2009] and *Gabriel et al.* [2012] suggest that the steady pulses are not stable, and thus, a time-dependent rupture model will not select one of the steady pulse solutions presented here. However, it is important to note that neither *Noda et al.* [2009] nor *Gabriel et al.* [2012] accounted for thermal decomposition. It is possible that the complicated phase diagram shown in Figure 4 may lead to stable steady pulses that trigger thermal decomposition, though this can only be tested using a model for a nonsteady rupture that accounts for thermal decomposition.

Even if the steady slip pulse solutions never emerge from more realistic rupture models we expect many of our conclusions to hold. We still expect thermal decomposition to become important when the temperature reaches θ_{lower} and the activation of thermal decomposition to lead to a longer slip duration and a larger total slip. Furthermore, we expect P_r/E_r to control the additional weakening triggered by the onset of thermal decomposition, and χ to control the amount of time spent at the peak temperature.

8. Conclusions

In this paper we produced the first dynamic rupture simulations to account for thermal decomposition. We studied the balance between thermal pressurization and thermal decomposition, showing that this balance can change significantly with background stress. In addition, we demonstrated that thermal decomposition can provide as much total weakening as thermal pressurization during a dynamic rupture.

Our results show that the activation of thermal decomposition significantly alters the rupture properties, leading to longer slip durations, larger total slips, and smaller rupture velocities. Furthermore, we showed that for some background stress thermal decomposition leads to distinctive along-fault slip rate profiles with peak slip rates near the trailing edge of the slip pulse, coinciding with the onset of the reaction.

We showed that accounting for thermal decomposition allows multiple self-healing slip pulse solutions to exist at a given background stress. Some of these solutions correspond to different balances between thermal pressurization, thermal decomposition, and hydrothermal diffusion, while other solutions correspond to triggering a single reaction multiple times, leading to a "train" of slip pulses. The wide range of possible rupture modes highlights the importance of coupling models for dynamic rupture with realistic models for nucleation, which may allow us to determine which of the many rupture modes is selected by a fault.

Based on our results, we highlighted two key parameters that are expected to control the impact of thermal decomposition. First, we showed that the additional weakening associated with thermal decomposition is largely controlled by the ratio P_r/E_r and presented a physical motivation for this ratio. Second, we showed that the ratio of hydraulic and thermal diffusivities χ plays an important role in controlling the amount of weakening produced by thermal decomposition. This is in stark contrast with the results for thermal pressurization alone, which are insensitive to changes in χ.

Appendix A: Nondimensionalization

To nondimensionalize our model we use the scalings from *Garagash* [2012]. First, we normalize the along-fault distance x using the slip pulse length L and normalize the across-fault coordinated y using the deforming zone thickness W. Next we normalize the slip δ using the characteristic slip-weakening distance for thermal pressurization under undrained and adiabatic conditions $\delta_c = \rho c W/f\Lambda$. Finally, we use the ambient effective stress to normalize the pore pressure rise and the maximum temperature rise $(\sigma_n - p_a)/\Lambda$ for a uniformly sheared gouge undergoing thermal pressurization under undrained and adiabatic conditions to normalize the temperature. This leads to

$$x = \frac{L}{2}(\tilde{x} + 1) \quad , \quad y = W\tilde{y} \quad , \quad \delta = \frac{\rho c W}{f\Lambda}\tilde{\delta} \tag{A1}$$

$$p = p_a + (\sigma_n - p_a)\tilde{p} \quad , \quad \theta = \frac{\sigma_n - p_a}{\Lambda}\tilde{\theta}, \tag{A2}$$

where we have used tildes to indicate dimensionless variables. Inserting the scalings for δ and x into the formula for the slip rate

$$V(x) = v_r \frac{\partial \delta}{\partial x} \tag{A3}$$

we can find the scaling for the slip rate,

$$V(x) = 2\frac{v_r \delta_c}{L}\tilde{V}(\tilde{x}) \quad , \quad \tilde{V}(\tilde{x}) = \frac{\partial \tilde{\delta}}{\partial \tilde{x}} \tag{A4}$$

Inserting this scaling into the integral equation linking the stress on the fault to the slip rate—equation (12)—we find a dimensionless integral equation for the stress along the fault as well as a scaling for the slip pulse length L,

$$\tilde{\tau}(\tilde{x}) = \tilde{\tau}_b - \frac{1}{\pi \tilde{L}} \int_{-1}^{1} \frac{\tilde{V}(s)}{\tilde{x} - s} \mathrm{d}s \tag{A5}$$

$$\tilde{L} = \frac{L}{\bar{\mu}\delta_c / f(\sigma_n - p_a)} \quad , \quad \tilde{\tau}_b = \frac{\tau_b}{f(\sigma_n - p_a)}. \tag{A6}$$

The first dimensionless parameter in the model is $\tilde{\tau}_b$, which measures the proximity of the background stress τ_b to the initial strength of the gouge layer $\tau_0 = f(\sigma_n - p_a)$. Using the slip rate scaling in the equations for conservation of energy and pore fluid mass, we find the two dimensionless equations,

$$\frac{\partial \tilde{\theta}}{\partial \tilde{x}} = \tilde{\tau}_f \tilde{V} \exp\left(-\pi \tilde{y}^2\right) + \frac{T_{\text{pulse}}}{8T^*} \frac{1}{(1+\sqrt{\chi})^2} \frac{\partial^2 \tilde{\theta}}{\partial \tilde{y}^2} - R_{\text{th}} \frac{T_{\text{pulse}}}{T^*} \exp\left(-\frac{K}{\tilde{\theta}_{\text{mp}}}\right) \exp\left(-\pi \beta^2 \tilde{y}^2\right), \tag{A7}$$

$$\frac{\partial \tilde{p}}{\partial \tilde{x}} = \frac{\partial \tilde{\theta}}{\partial \tilde{x}} + \frac{T_{\text{pulse}}}{8T^*} \frac{\chi}{(1+\sqrt{\chi})^2} \frac{\partial^2 \tilde{p}}{\partial \tilde{y}^2} + R_{\text{hy}} \frac{T_{\text{pulse}}}{T^*} \exp\left(-\frac{K}{\tilde{\theta}_{\text{mp}}}\right) \exp\left(-\pi \beta^2 \tilde{y}^2\right), \tag{A8}$$

and four more dimensionless parameters

$$\chi = \frac{\alpha_{\text{hy}}}{\alpha_{\text{th}}} \quad , \quad K = \frac{Q\Lambda}{R(\sigma_n - p_a)} \quad , \quad R_{\text{th}} = \frac{\bar{m} E_r \Lambda T^* A}{2(\sigma_n - p_a)} \quad , \quad R_{\text{hy}} = \frac{\bar{m} P_r T^* A}{2(\sigma_n - p_a)} \tag{A9}$$

Another dimensionless parameter is needed to extract the rupture velocity—and thus the slip pulse length—from the dimensionless solutions. As shown in *Garagash* [2012] this parameter is v^*/c_s where c_s is the shear wave speed and v^* is a characteristic rupture velocity defined by

$$v^* = \frac{\mu}{\tau_0} \frac{\delta_c}{T^*} = \frac{\mu}{\tau_0} \frac{\rho c}{f\Lambda} \frac{4\alpha}{W} \tag{A10}$$

As will be shown in the next section, the slip duration of a self-healing slip pulse T_{sh} is solved for using the self-healing condition $k_L = 0$, so our dimensionless problem is controlled by seven dimensionless parameters. These are $\tilde{\tau}_b$, χ, K, R_{th}, R_{hy}, v^*/c_s, and the scaled initial temperature,

$$\tilde{\theta}_a = \frac{\theta_a}{(\sigma_n - p_a)/\Lambda}. \tag{A11}$$

Motivated by the definitions of α and χ, which measure the total impact of hydrothermal diffusion and the balance between hydraulic and thermal diffusion, respectively, rather than quantifying the impact of hydraulic and thermal diffusion separately, we can recast the two dimensionless parameters R_{th} and R_{hy} in the following form,

$$R_{\text{react}} = \left(\sqrt{R_{\text{th}}} + \sqrt{R_{\text{hy}}}\right)^2 = \frac{\bar{m} T^* A}{2(\sigma_n - p_a)} \left(\sqrt{\Lambda E_r} + \sqrt{P_r}\right)^2 \tag{A12}$$

$$X = \frac{P_r}{\Lambda E_r} \tag{A13}$$

Here R_{react} measures the total impact of the decomposition reaction, and X measures the balance between the temperature rise buffered and the pore pressure generated by the reaction. Using these new definitions, we find,

$$R_{th} = \frac{1}{(1+\sqrt{X})^2} R_{react} \quad , \quad R_{hy} = \frac{X}{(1+\sqrt{X})^2} R_{react} \tag{A14}$$

Note that when $X = 1$ the shear strength evolution for uniform shear under undrained and adiabatic conditions is identical to the solution for thermal pressurization alone from *Lachenbruch* [1980]. The natural appearance of the parameter X further justifies our interpretation of P_r/E_r as an effective value of Λ that can be used to crudely estimate how much dynamic weakening a specific reaction will provide. The two parameter sweeps over E_r and P_r shown in Figures 9 and 10 vary one of R_{th} and R_{hy} while keeping the other one constant. We also performed parameter sweeps that fix R_{react} and vary X finding very similar results to those shown in Figures 9 and 10. As X increases—corresponding to a larger value of P_r/E_r—the effects of thermal decomposition become more pronounced.

Appendix B: Numerical Methods

Here we outline the numerical method used to solve for steady slip pulses propagating at a constant rupture velocity, closely following the numerical method used in *Viesca and Garagash* [2012] and outlined in *Viesca and Garagash* [2015]. For simplicity this is done for the dimensionless model from Appendix A, and to reduce notation we drop the tildes used to denote dimensionless variables.

B1. Green's Function Formulation for Integral Equations

To begin we define the dimensionless diffusivities in equations (A7) and (A8),

$$D_{th} = \frac{T_{pulse}}{8T^*} \frac{1}{(1+\sqrt{\chi})^2} \quad , \quad D_{hy} = \frac{T_{pulse}}{8T^*} \frac{\chi}{(1+\sqrt{\chi})^2}, \tag{B1}$$

allowing us to write the equations for temperature and pore pressure in matrix form as

$$\begin{pmatrix} \theta \\ p \end{pmatrix}_x = \begin{pmatrix} \omega_\theta \\ \omega_\theta + \omega_p \end{pmatrix} + \begin{pmatrix} D_{th} & 0 \\ D_{th} & D_{hy} \end{pmatrix} \begin{pmatrix} \theta \\ p \end{pmatrix}_{yy}, \tag{B2}$$

where ω_θ are the source terms from frictional heating and thermal decomposition in the energy equation and ω_p is the source term from thermal decomposition in the pore pressure equation. Next we use the matrix diagonalization,

$$\begin{pmatrix} D_{th} & 0 \\ D_{th} & D_{hy} \end{pmatrix} = \frac{1}{D_{th}-D_{hy}} \begin{pmatrix} D_{th}-D_{hy} & 0 \\ D_{th} & 1 \end{pmatrix} \begin{pmatrix} D_{th} & 0 \\ 0 & D_{hy} \end{pmatrix} \begin{pmatrix} 1 & 0 \\ -D_{th} & D_{th}-D_{hy} \end{pmatrix}, \tag{B3}$$

which is valid when $D_{th} \neq D_{hy}$, to decouple our pair of diffusion equations. This leads to

$$\begin{pmatrix} \theta \\ \Pi \end{pmatrix}_x = \begin{pmatrix} \omega_\theta \\ \frac{D_{hy}}{D_{hy}-D_{th}}\omega_\theta + \omega_p \end{pmatrix} + \begin{pmatrix} D_{th} & 0 \\ 0 & D_{hy} \end{pmatrix} \begin{pmatrix} \theta \\ \Pi \end{pmatrix}_{yy}, \tag{B4}$$

where we have defined,

$$\Pi = p + \frac{D_{th}}{D_{hy}-D_{th}} T. \tag{B5}$$

The decoupled diffusion equations can now be solved independently using the Green's function,

$$G(x-x', y-y'; \alpha) = \frac{1}{\sqrt{4\pi\alpha(x-x')}} \exp\left(-\frac{(y-y')^2}{4\alpha(x-x')}\right). \tag{B6}$$

This leads to the solutions for θ and Π on the fault plane $y = 0$,

$$\theta_{mp}(x) = \tilde{\theta}_a + \int_{-1}^{x} \int_{-\infty}^{\infty} G(x-x', y'; D_{th}) \omega_\theta(x', y') \mathrm{d}y' \mathrm{d}x', \tag{B7}$$

$$\Pi_{mp}(x) = \int_{-1}^{x}\int_{-\infty}^{\infty} G(x-x',y';D_{\mathrm{hy}})\left(\omega_p(x',y') + \frac{D_{\mathrm{hy}}}{D_{\mathrm{hy}}-D_{\mathrm{th}}}\omega_\theta(x',y')\right)\mathrm{d}y'\mathrm{d}x', \tag{B8}$$

Following *Viesca and Garagash* [2015], we now take advantage of the fact that the integrals over y' can be done exactly. For example, we will show how this works for the integral representing the frictional heating term in the heat equation

$$\int_{-1}^{x}\int_{-\infty}^{\infty} \frac{\tau(x')V(x')}{\sqrt{4\pi D_{\mathrm{th}}(x-x')}} \exp\left(-\pi y'^2\right)\exp\left(-\frac{y'^2}{4D_{\mathrm{th}}(x-x')}\right)\mathrm{d}y'\mathrm{d}x'. \tag{B9}$$

Combining the exponentials and separating the integrals over y' and x', we find

$$\int_{-1}^{x} \frac{\tau(x')V(x')}{\sqrt{4\pi D_{\mathrm{th}}(x-x')}} \int_{-\infty}^{\infty} \exp\left(-\frac{1+4\pi D_{\mathrm{th}}(x-x')}{4D_{th}(x-x')}y'^2\right)\mathrm{d}y'\mathrm{d}x'. \tag{B10}$$

The integral over y' can be done exactly leading to

$$\int_{-1}^{x} \frac{\tau(x')V(x')}{\sqrt{1+4\pi D_{\mathrm{th}}(x-x')}}\mathrm{d}x'. \tag{B11}$$

The other integrals in equations (B7) and (B8) can be done in a similar fashion, leading to the equations for the pore pressure and temperature on $y = 0$,

$$\theta_{\mathrm{mp}}(x) = \tilde{\theta}_a + \int_{-1}^{1} \hat{A}(x-x')\tau(x')V(x') + \hat{B}(x-x')\exp\left(-\frac{K}{\theta_{\mathrm{mp}}(x')}\right)\mathrm{d}x', \tag{B12}$$

$$p_{\mathrm{mp}}(x) = \int_{-1}^{1} \hat{C}(x-x')\tau(x')V(x') + \hat{D}(x-x')\exp\left(-\frac{K}{\theta_{\mathrm{mp}}(x')}\right)\mathrm{d}x', \tag{B13}$$

where the functions A, B, C, and D are defined as

$$\hat{A} = \frac{H(x-x')}{\sqrt{1+4\pi D_{\mathrm{th}}(x-x')}} \quad , \quad \hat{B} = -R_{\mathrm{th}}\frac{H(x-x')}{\sqrt{1+4\pi\beta D_{\mathrm{th}}(x-x')}}, \tag{B14}$$

$$\hat{C} = \frac{H(x-x')}{D_{\mathrm{hy}}-D_{\mathrm{th}}}\left(\frac{D_{\mathrm{hy}}}{\sqrt{1+4\pi D_{\mathrm{hy}}(x-x')}} - \frac{D_{\mathrm{th}}}{\sqrt{1+4\pi D_{\mathrm{th}}(x-x')}}\right) \tag{B15}$$

$$\hat{D} = \left(R_{\mathrm{hy}} - \frac{D_{\mathrm{hy}}R_{\mathrm{th}}}{D_{\mathrm{hy}}-D_{th}}\right)\frac{H(x-x')}{\sqrt{1+4\pi\beta D_{\mathrm{hy}}(x-x')}} + \frac{D_{\mathrm{th}}R_{\mathrm{th}}}{D_{\mathrm{hy}}-D_{\mathrm{th}}}\frac{H(x-x')}{\sqrt{1+4\pi\beta D_{\mathrm{th}}(x-x')}}, \tag{B16}$$

and H is the Heaviside function. Functions similar to $\hat{A}$ and $\hat{C}$ where previously used by *Andrews* [2002] to model thermal pressurization alone.

Next we use the pore pressure on the midplane predicted by equation (B13) to find the fault strength

$$\tau_f(x) = 1 - \int_{-1}^{1} \hat{C}(x-x')\tau(x')V(x') + \hat{D}(x-x')\exp\left(-\frac{K}{\theta_{\mathrm{mp}}(x')}\right)\mathrm{d}x', \tag{B17}$$

We know that within the slipping region $x \in [0, L]$ this strength must be equal to the shear stress predicted by equation (A5) leading to the integral equation,

$$1 - \int_{-1}^{1} \hat{C}(x-x')\tau(x')V(x') + \hat{D}(x-x')\exp\left(-\frac{K}{\theta_{\mathrm{mp}}(x')}\right)\mathrm{d}x' = \tilde{\tau}_b - \frac{1}{\pi L}\int_{-1}^{1}\frac{V(\xi)}{x-\xi}\mathrm{d}\xi \tag{B18}$$

A second integral equation can be found using the conservation of energy accounting for thermal decomposition,

$$\theta_{\mathrm{mp}}(x) = \tilde{\theta}_a + \int_{-1}^{1} \widehat{A}(x-x')\tau(x')V(x') + \widehat{B}(x-x') \exp\left(-\frac{K}{\theta_{\mathrm{mp}}(x')}\right) \mathrm{d}x', \tag{B19}$$

In the next subsection we solve this pair of integral equations for the slip rate and temperature profiles within the slip pulse as well as the slip pulse length and slip duration.

B2. Solution Using Gauss-Chebyshev Quadrature

To solve this pair of integral equations we use the numerical methods outlined in *Viesca and Garagash* [2012] and *Viesca and Garagash* [2015], which combine the Green's function approach from *Garagash* [2012] with the Gauss-Chebyshev quadrature methods for singular integral equations from *Erdogan and Gupta* [1972] and *Erdogan et al.* [1973]. To begin we define the two sets of Chebyshev nodes

$$x_i = \cos\left(\frac{2i-1}{n+1}\frac{\pi}{2}\right) \quad , \quad i = 1, \ldots, n+1, \tag{B20}$$

$$x_j = \cos\left(\frac{j}{n+1}\pi\right) \quad , \quad j = 1, \ldots, n. \tag{B21}$$

The set of points x_j are the base for the Gauss-Chebyshev quadrature rule,

$$\int_{-1}^{+1} \sqrt{1-x^2} f(x) \mathrm{d}x = \sum_{j=1}^{n} w_j f(x_j), \tag{B22}$$

with the weights,

$$w_j = \frac{\pi}{n+1} \sin^2\left(\frac{j}{n+1}\pi\right). \tag{B23}$$

Defining the function $v(x)$ through $V(x) = \sqrt{1-x^2}\, v(x)$, we can write the stress at the points x_i as

$$\tau_i = \tilde{\tau}_b - \frac{1}{L} K_{ij} v_j \quad , \quad K_{ij} = \frac{w_j}{\pi(x_i - x_j)}. \tag{B24}$$

The Gauss-Chebyshev quadrature is next used to evaluate the fault strength, leading to

$$\tau_i = 1 - C_{ij}(\tau v)_j - D_{ij} \exp\left(-\frac{K}{\theta_j}\right), \tag{B25}$$

where

$$C_{ij} = w_j C(x_i - x_j) \quad , \quad D_{ij} = \frac{w_j D(x_i - x_j)}{\sqrt{1-x_j^2}}. \tag{B26}$$

Setting the fault stress from equation (B24) equal to the fault strength from equation (B25) at every point of the x_i grid, we obtain $n+1$ equations. More equations can be obtained by applying the quadrature to the integral equation modeling the conservation of energy. This leads to

$$\tilde{\theta}_i = \tilde{\theta}_a + A_{ij}(\tau v)_j + B_{ij} \exp\left(-\frac{K}{\theta_j}\right), \tag{B27}$$

$$A_{ij} = w_j A(x_i - x_j) \quad , \quad B_{ij} = \frac{w_j B(x_i - x_j)}{\sqrt{1-x_j^2}}. \tag{B28}$$

Note that to evaluate equations (B25) and (B27) we must know τ on the x_j grid, but equation (B25) gives us the shear stress on the x_i grid. Similarly, in equation (B27) we require the temperature profile on the x_j grid,

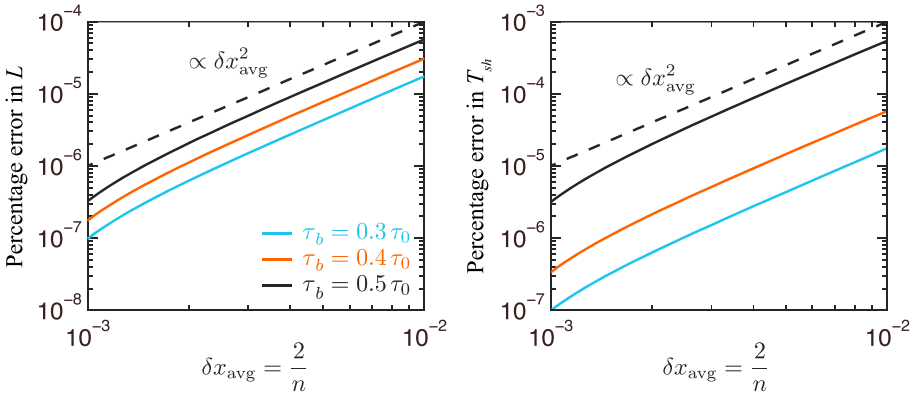

Figure B1. A plot showing a convergence test for the numerical scheme outlined in Appendix B. This test was done using the parameters in Table 1 and three different values of the background stress τ_b. We see that the method is second order and the percentage error in $T_{\rm sh}$ and L is small once $n > 1000$. The majority of the simulations in this paper are done using $n = 1000$, with a few higher resolutions for the smallest values of τ_b where slip is confined to a small zone immediately adjacent to the rupture tip.

yet equation (B27) gives us the temperature profile on the x_i grid. To move between the two grids we use the barycentric Lagrange interpolation matrix

$$I_{ji} = \left(\frac{w_i}{x_j - x_i}\right) \Big/ \sum_{m=1}^{n+1} \frac{w_{i=m}}{x_j - x_{i=m}} \quad , \quad w_i = (-1)^{i-1} \sin\left(\frac{\pi}{2}\frac{2i-1}{n+1}\right), \tag{B29}$$

which is accurate and efficient for functions approximated on Chebyshev nodes [*Berrut and Trefethen*, 2004]. Equations (B25) and (B27) lead to a nonlinear system of $2n + 1$ equations, where $n + 1$ come from setting the stress equal to the strength on the x_i grid and the other n coming from multiplying equation (B27) by I_{ji} to find a consistent temperature profile on the x_j grid. This nonlinear system can be solved for v on the x_j grid, θ on the x_j grid, and L using Newton-Raphson iteration. Once a solution is found we calculate k_L using

$$k_L = -\frac{4}{\pi\sqrt{L}} \int_{-1}^{1} \sqrt{\frac{x}{1-x}} \frac{\mathrm{d}\tau}{\mathrm{d}x} \mathrm{d}x. \tag{B30}$$

Repeating this for many imposed slip durations leads to k_L as a function of $T_{\rm pulse}/T^*$. This curve is then tracked until k_L vanishes and a self-healing solution is found.

Another slightly more complicated method that we use extensively in this paper includes the dimensionless self-healing condition $k_L = 0$ in the Newton-Raphson iteration. This leads to one additional equation that is used to solve for the slip duration $T_{\rm sh}$ at which self-healing occurs. This second method is found to be much more computationally efficient and is used to generate the majority of the results in this paper.

We perform a convergence test on the system above for several values of the background stress τ_b and the parameters from Table 1. The results from this convergence test are shown in Figure B1. We see that the method is second order and that the percentage error in the values of $T_{\rm sh}$ and L at which self-healing occurs is acceptable when $n > 400$. To ensure small errors for a wider range of τ_b, the majority of calculations in this paper are performed with $n = 1000$, though sometimes we use a higher value of n at the lowest values of τ_b where the slip is confined to a narrow zone very close to the rupture tip.

Appendix C: Validation of Reaction Kinetics Approximation

The Green's function solution outlined above relies on approximating the reaction kinetics in the deforming zone as the product of the reaction kinetic on $y = 0$ and an assumed Gaussian shape in the across-fault direction. Here we test this approximation by replacing equations (5) and (7) with

$$v_r \frac{\partial \theta}{\partial x} = \frac{\tau_f \dot{\gamma}}{\rho c} + \alpha_{th} \frac{\partial^2 \theta}{\partial y^2} - \bar{m} E_r \exp\left(-\frac{Q}{R\theta}\right) \tag{C1}$$

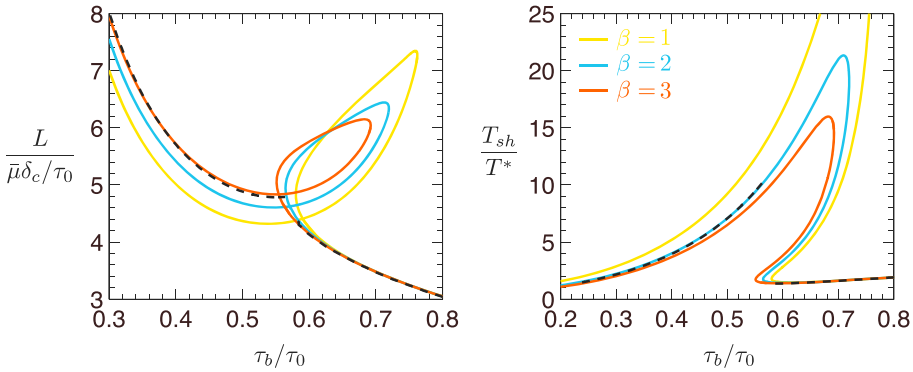

Figure C1. A plot showing how the results from the Newton-Raphson method outlined in Appendix B compare with the finite difference simulations outlined in Appendix C. These results were produced using the parameters given in Table 1. The good agreement between the two methods validates our assumptions about the reacting zone shape. We see that for the dimensionless slip pulse length the best agreement occurs for $\beta = 3$, and for the dimensionless slip duration the best agreement occurs for $\beta = 2$. Based on these plots, we choose an optimal value of $\beta = 2$, which is used in all other simulations in this paper.

$$v_r \frac{\partial p}{\partial x} = v_r \Lambda \frac{\partial \theta}{\partial x} + \alpha_{hy} \frac{\partial^2 p}{\partial y^2} + \bar{m} P_r \exp\left(-\frac{Q}{R\theta}\right) \tag{C2}$$

Note that these equations make no assumptions about the shape of the reacting zone, and the reaction rate is calculated for all y using the temperature at that location.

These equations are solved numerically via an iterative procedure that starts with a velocity profile $V(x)$ and solves for the shear strength and temperature evolution within the pulse using finite differences. Assuming that the shear strength and shear stress are equal within the slip pulse, this new shear strength profile can be used to predict a new slip rate profile using [*Rice*, 1968; *Garagash*, 2012]

$$V(x) = \frac{2}{\pi} \frac{v_r}{\bar{\mu}} \int_0^L \sqrt{\frac{x(L-x)}{\xi(L-\xi)}} \quad \tau(\xi) \frac{\mathrm{d}\xi}{x-\xi}. \tag{C3}$$

This new slip rate profile is then used as the input for the next finite difference calculation, and we continue to iterate until the difference between the slip rate profile used to drive the finite difference calculation and the new slip rate profile predicted by equation (C3) agree to within a small tolerance, which is typically assumed to be $\sim 10^{-4} - 10^{-3}$ in dimensionless units.

Figure C1 shows how the method that makes no assumption about the reacting zone shape compares with the method that assumes a reacting zone with a Gaussian shape and fixed thickness for different values of β. We see good agreement between the two methods with the best agreement in the value of T_{sh} occurring for $\beta = 2$ and the best agreement in L occurring for $\beta = 3$. These observations validate the assumptions made about the shape of the reacting zone and suggest an optimal value of $\beta = 2$. This value of β is used for the rest of the calculations presented in this paper.

Acknowledgments
We are grateful for support by NSF Geophysics Program grant EAR-1315447 to Harvard University, and for supplemental support by the Southern California Earthquake Center (SCEC) funded by NSF cooperative agreement EAR-1033462 and USGS cooperative agreement G12AC20038. This is SCEC contribution 6000. D.G. is grateful for support from Harvard University while on sabbatical leave with Jim Rice's group there (Winter 2012). R.V. is grateful for postdoctoral support from Dalhousie University via NSF grant EAR-1036985 to D.G.

References

Andrews, D. J. (2002), A fault constitutive relation accounting for thermal pressurization of pore fluid, *J. Geophys. Res.*, *107*(B12), 2363, doi:10.1029/2002JB001942.

Berrut, J.-P., and L. N. Trefethen (2004), Barycentric Lagrange interpolation, *SIAM Rev.*, *46*(3), 501–517.

Bizzarri, A., and M. Cocco (2006), A thermal pressurization model for the spontaneous dynamic rupture propagation on a three-dimensional fault: 2. Traction evolution and dynamic parameters, *J. Geophys. Res.*, *111*, B05304, doi:10.1029/2005JB003864.

Brantut, N., and J. R. Rice (2011), Decomposition-induced overpressures and fault zone dilation during earthquake slip, Abstract T23G-06 presented at 2011 Fall Meeting, AGU, San Francisco, Calif., 5–9 Dec.

Brantut, N., and J. Sulem (2012), Strain localization and slip instability in a strain-rate hardening, chemically weakening material, *J. Appl. Mech.*, *79*(3), 31004, doi:10.1115/1.4005880.

Brantut, N., A. Schubnel, J.-N. Rouzaud, F. Brunet, and T. Shimamoto (2008), High-velocity frictional properties of a clay-bearing fault gouge and implications for earthquake mechanics, *J. Geophys. Res.*, *113*, B10401, doi:10.1029/2007JB005551.

Brantut, N., A. Schubnel, J. Corvisier, and J. Sarout (2010), Thermochemical pressurization of faults during coseismic slip, *J. Geophys. Res.*, *115*, B05314, doi:10.1029/2009JB006533.

Brantut, N., R. Han, T. Shimamoto, N. Findling, and A. Schubnel (2011), Fast slip with inhibited temperature rise due to mineral dehydration: Evidence from experiments on gypsum, *Geology*, *39*(1), 59–62.

Broberg, K. B. (1978), On transient sliding motion, *Geophys. J. Int.*, *52*(3), 397–432.
Bullock, R. J., N. De Paola, R. E. Holdsworth, and J. Trabucho-Alexandre (2014), Lithological controls on the deformation mechanisms operating within carbonate-hosted faults during the seismic cycle, *J. Struct. Geol.*, *58*, 22–42.
Byerlee, J. (1978), Friction of rocks, *Pure Appl. Geophys.*, *116*(4-5), 615–626.
Coker, D., G. Lykotrafitis, A. Needleman, and A. J. Rosakis (2005), Frictional sliding modes along an interface between identical elastic plates subject to shear impact loading, *J. Mech. Phys. Solids*, *53*, 884–922.
Collettini, C., C. Viti, T. Tesei, and S. Mollo (2013), Thermal decomposition along natural carbonate faults during earthquakes, *Geology*, *41*, 927–930.
De Paola, N., T. Hirose, T. Mitchell, G. Di Toro, C. Viti, and T. Shimamoto (2011), Fault lubrication and earthquake propagation in thermally unstable rocks, *Geology*, *39*(1), 35–38, doi:10.1130/G31398.1.
Di Toro, G., R. Han, T. Hirose, N. De Paola, S. Nielsen, K. Mizoguchi, F. Ferri, M. Cocco, and T. Shimamoto (2011), Fault lubrication during earthquakes, *Nature*, *471*, 494–498, doi:10.1038/nature09838.
Dollimore, D., P. Tong, and K. S. Alexander (1996), The kinetic interpretation of the decomposition of calcium carbonate by use of relationships other than the Arrhenius equation, *Thermochim. Acta*, *282-283*, 13–27.
Erdogan, F., and G. D. Gupta (1972), On the numerical solution of singular integral equations, *Quart. Appl. Math.*, *30*, 525–534.
Erdogan, F., G. D. Gupta, and T. S. Cook (1973), Numerical solution of singular integral equations, in *Mechanics of Fracture*, vol. 1, edited by G. C. Sih, chap. 7, pp. 368–425, Noordhoff Int., Leyden, Netherlands.
Freund, L. B. (1979), The mechanics of dynamic shear crack propagation, *J. Geophys. Res.*, *84*, 2199–2209.
Fulton, P. M., et al. (2013), Low coseismic friction on the Tohoku-Oki fault determined from temperature measurements, *Science*, *342*, 1214–1217, doi:10.1126/science.1243641.
Gabriel, A.-A., J.-P. Ampuero, L. A. Dalguer, and P. M. Mai (2012), The transition of dynamic rupture styles in elastic media under velocity-weakening friction, *J. Geophys. Res.*, *117*, B09311, doi:10.1029/2012JB009468.
Garagash, D. I. (2012), Seismic and aseismic slip pulses driven by thermal pressurization of pore fluid, *J. Geophys. Res.*, *117*, B04314, doi:10.1029/2011JB008889.
Garagash, D. I., and J. W. Rudnicki (2003), Shear heating of a fluid-saturated slip-weakening dilatant fault zone 1: Limiting regimes, *J. Geophys. Res.*, *108*, 2121–2139, doi:10.1029/2001JB001653.
Goldsby, D. L., and T. E. Tullis (2011), Flash heating leads to low frictional strength of crustal rocks at earthquake slip rates, *Science*, *334*, 216–218, doi:10.1126/science.1207902.
Han, R., T. Shimamoto, T. Hirose, J. Ree, and J. Ando (2007a), Ultra-low friction of carbonate faults caused by thermal decomposition, *Science*, *316*(5826), 878–881.
Han, R., T. Shimamoto, J. Ando, and J. Ree (2007b), Seismic slip record in carbonate-bearing fault zones: An insight from high-velocity friction experiments on siderite gouge, *Geology*, *35*(12), 1131–1134.
Heaton, T. H. (1990), Evidence for and implications of self-healing pulses of slip in earthquake rupture, *Phys. Earth Planet. Inter.*, *64*, 1–20.
Hirose, T., and M. Bystricky (2007), Extreme dynamic weakening of faults during dehydration by coseismic shear heating, *Geophys. Res. Lett.*, *34*, L14311, doi:10.1029/2007GL030049.
Lachenbruch, A. H. (1980), Frictional heating, fluid pressure, and the resistance to fault motion, *J. Geophys. Res.*, *85*, 6097–6112.
Lachenbruch, A. H., and J. H. Sass (1980), Heat flow and energetics of the San Andreas fault zone, *J. Geophys. Res.*, *85*, 6185–6222.
Lapusta, N. (2005), Modes of dynamic rupture on interfaces with nonlinear rate and state friction laws, paper presented at 11th International Conference Fracture, Curran Associates, Inc., Turin, Italy, 20–25 March.
Mase, C. W., and L. Smith (1985), Pore-fluid pressures and frictional heating on a fault surface, *Pure Appl. Geophys.*, *92*, 6249–6272.
Mase, C. W., and L. Smith (1987), Effects of frictional heating on the thermal, hydrologic, and mechanical response of a fault, *J. Geophys. Res.*, *92*, 6249–6272.
Noda, H., and N. Lapusta (2010), Three-dimensional earthquake sequence simulations with evolving temperature and pore pressure due to shear heating: Effect of heterogeneous hydraulic diffusivity, *J. Geophys. Res.*, *115*, B12314, doi:10.1029/2010JB007780.
Noda, H., and N. Lapusta (2013), Stable creeping fault segments can become destructive as a result of dynamic weakening, *Nature*, *493*, 518–521, doi:10.1038/nature11703.
Noda, H., E. M. Dunham, and J. R. Rice (2009), Earthquake ruptures with thermal weakening and the operation of major faults at low overall stress levels, *J. Geophys. Res.*, *114*, B07302, doi:10.1029/2008JB006143.
Perrin, G., J. R. Rice, and G. Zheng (1995), Self-healing slip pulse on a frictional surface, *J. Mech. Phys. Solids*, *43*, 1461–1495.
Platt, J. D., J. W. Rudnicki, and J. R. Rice (2014), Stability and localization of rapid shear in fluid-saturated fault gouge, 2. Localized zone width and strength evolution, *J. Geophys. Res. Solid Earth*, *119*, 4334–4359, doi:10.1002/2013JB010711.
Platt, J. D., N. Brantut, and J. R. Rice (2015), Strain localization driven by thermal decomposition during seismic shear, *J. Geophys. Res.*, *120*, 4405–4433, doi:10.1002/2014JB011493.
Poulet, T., E. Veveakis, K. Regenauer-Lieb, and D. A. Yuen (2014), Thermo-poro-mechanics of chemically active creeping faults: 3. The role of serpentinite in episodic tremor and slip sequences, and transition to chaos, *J. Geophys. Res. Solid Earth*, *119*, 4606–4625, doi:10.1002/2014JB011004.
Proctor, B. P., T. M. Mitchell, G. Hirth, D. Goldsby, F. Zorzi, J. D. Platt, and G. Di Toro (2014), Dynamic weakening of serpentinite gouges and bare-surfaces at seismic slip rates, *J. Geophys. Res. Solid Earth*, *119*, 8107–8131, doi:10.1002/2014JB011057.
Rempel, A. W., and J. R. Rice (2006), Thermal pressurization and onset of melting in fault zones, *J. Geophys. Res.*, *111*, B09314, doi:10.1029/2006JB004314.
Rice, J. R. (1968), Mathematical analysis in the mechanics of fracture, in *Fracture, an Advanced Treatise*, vol. 2, edited by H. Liebowitz, chap. 3, pp. 191–311, Academic, New York.
Rice, J. R. (1999), Flash heating at asperity contacts and rate-dependent friction, *EoS Trans. AGU*, *80*(46), Fall Meet. Suppl., F681.
Rice, J. R. (2006), Heating and weakening of faults during earthquake slip, *J. Geophys. Res.*, B05311, doi:10.1029/2005JB004006.
Rice, J. R., C. G. Sammis, and R. Parsons (2005), Off-fault secondary failure induced by a dynamic slip-pulse, *Bull. Seismol. Soc. Am.*, *95*(1), 109–134, doi:10.1785/0120030166.
Rice, J. R., J. W. Rudnicki, and J. D. Platt (2014), Stability and localization of rapid shear in fluid-saturated fault gouge: 1. Linearized stability analysis, *J. Geophys. Res.*, *119*, 4311–4333, doi:10.1002/2013JB010710.
Shi, Z., Y. Ben-Zion, and A. Needleman (2008), Properties of dynamic rupture and energy partition in a solid with a frictional interface, *J. Mech. Phys. Solids*, *56*, 5–24.
Smith, S. A. F., G. Di Toro, S. Kim, J.-H. Ree, S. Nielsen, A. Billi, and R. Spiess (2013), Coseismic recrystallization during shallow earthquake slip, *Geology*, *41*, 63–66, doi:10.1130/G33588.1.

Sulem, J., and V. Famin (2009), Thermal decomposition of carbonates in fault zones: Slip-weakening and temperature-limiting effects, *J. Geophys. Res.*, *114*, B03309, doi:10.1029/2008JB006004.

Sulem, J., V. Famin, and H. Noda (2009), Correction to "Thermal decomposition of carbonates in fault zones: Slip-weakening and temperature-limiting effects", *J. Geophys. Res.*, *114*, B06311, doi:10.1029/2009JB006576.

Townend, J., and M. D. Zoback (2004), Regional tectonic stress near the San Andreas fault in central and southern California, *Geophys. Res. Lett.*, *31*, L15S11, doi:10.1029/2003GL018918.

Urata, Y., K. Kuge, and Y. Kase (2012), Spontaneous dynamic rupture propagation beyond fault discontinuities: Effect of thermal pressurization, *Bull. Seismol. Soc. Am.*, *102*, 53–63, doi:10.1785/0120110089.

Urata, Y., S. Hok, E. Fukuyama, and R. Madariaga (2014), The effect of thermal pressurization on dynamic fault branching, *Geophys. J. Int.*, *196*, 1237–1246, doi:10.1093/gji/ggt457.

Viesca, R. C., and D. Garagash (2012), Steady slip pulses on faults with rate- and state-dependent friction and multiple thermal weakening mechanisms, Abstract S21B-2435 presented at 2012 Fall Meeting, AGU, San Francisco, Calif., 3–7 Dec.

Viesca, R. C., and D. Garagash (2015), Ubiquitous weakening of faults due to thermal pressurization, *Nat. Geosci.*, in press.

Weertman, J. (1980), Unstable slippage across a fault that separates elastic media of different elastic constants, *J. Geophys. Res.*, *85*, 1455–1461.

Wibberley, C. A. J., and T. Shimamoto (2003), Internal structure and permeability of major strike-slip fault zones: The Median Tectonic Line in Mie Prefecture, southwest Japan, *J. Struct. Geol.*, *25*, 59–78.

Yoffe, E. H. (1951), The moving griffith crack, *Philos. Mag.*, *42*(330), 739–750.

Zheng, G., and J. R. Rice (1998), Conditions under which velocity-weakening friction allows a self-healing versus a cracklike mode of rupture, *Bull. Seismol. Soc. Am.*, *88*(6), 1466–1483.